5.1 Introduction

The initial $m = 0$ RF current drive studies described in Section 5.4 are subsidiary to the main body of work presented in this thesis. However, it is felt that the results of these experiments are worthy of inclusion here, if only for the sake of completeness or the fact that these studies are not mentioned elsewhere. The reader may skip Section 5.4 without any loss of continuity in the main body of work concerning $m = 1$ helical RF current drive.

The results of RF current drive experiments using $m = 0$ external coil structures, the $m = 1$ double-helix antenna and the $m = +and-1$ helical mesh antenna are presented in this chapter.

Detailed magnetic probe measurements were used to study the steady magnetic field structure of reproducible discharges produced using the latter two types of external coil structures.

The theory presented in Chapter 2 has been developed in order to model the steady driven currents observed in the $m = 1$ double-helix antenna experiments. The vacuum RF magnetic field calculations for the $m = 1$ double-helix antenna presented in Chapter 2, have been extended to describe the vacuum fields produced by the $m = +and-1$ helical mesh antenna. However, a theoretical analysis of $m = +and-1$ helical mesh current drive (which is necessarily a 3-dimensional problem), remains to be given.

5.2 Experimental Procedure

The procedure for producing a discharge in each of the Rythmac devices was as follows.

1. The discharge vessel was evacuated to a base pressure of about 10^{-6} Torr.

2. Argon gas was allowed to flow continuously through the vessel; the filling pressure being controlled by a needle leak valve. For higher filling pressures, the butterfly valve immediately above the pump could be partially closed. This was desirable to reduce the flow rate required for a given filling gas pressure and to avoid choking the pump.

3. The line generator trigger units, diagnostics and data acquisition system were put into a standby state.

4. The steady toroidal field was applied.

5. The 'slow' capacitor bank vertical field coil power supply was charged to the appropriate voltage.

6. The line generators were charged to the preset working voltage.

7. The operator then initiated the plasma shot by firing the 'slow' capacitor bank. This resulted in the following sequence of events:

   (a) The slow capacitor bank was discharged through the vertical field coils.

   (b) A pulse derived from the rising vertical field coil current was used to trigger a Digital Delay Unit. [1]

   (c) An output of the Digital Delay Unit was used to trigger the RF sources at the time of peak vertical magnetic field.

   (d) Additional outputs of the Delay Unit were used to trigger each of the digital storage oscilloscopes which monitored the diagnostics. The timing of these outputs and the oscilloscope timebase was chosen so that the entire plasma shot was sampled.

[1] The Digital Delay Unit (DDU) was designed and constructed in the Flinders University Electronics Workshop.

8. The operator then disabled the line generator charging units. The diagnostic signals displayed on the oscilloscopes could now be examined. The first oscilloscope was used to display both line generator current waveforms. The second oscilloscope was used to display the output of the Rogowski belt which monitored the driven toroidal current. Magnetic probe signals were recorded on a third oscilloscope.

   If the operator was satisfied that the shot was taken with standard conditions (i.e. 90^0 phase difference between the line generators and correct filling pressure), the digitised data was recorded photographically and/or transferred to flexible disk. Non-standard shots were detected by visual inspection of the driven toroidal current waveform and the phasing between the RF line generator currents. Variations of the driven toroidal current from 'standard' could be traced to a cause such as a change in the filling gas pressure. The filling pressure was monitored regularly with a Datametrics Barocel gauge (Model 1173) and adjusted when necessary.

9. The system was then made ready for the next plasma shot by repeating the above sequence from step (5).

The discharge timing sequence outlined above is shown in Figure 5.1. The experiments were conducted with a cycle time of approximately one minute, which was governed mainly by the slow capacitor bank charging time and the time taken to transfer digitised data to floppy disk.

For the later experiments in Rythmac-3 where a DC vertical magnetic field was used, the above procedure was modified at steps (5) and (7). The operator now initiated the plasma shot at step (7b), by manually triggering the DDU.

It was observed that when the apparatus was reactivated after a period of inactivity (say 24 hours or longer), a number of 'cleaning' shots would be required before the discharges were reproducible. Good reproducibility was generally obtained after twenty or less cleaning shots. The irreproducibility during the initial discharges is

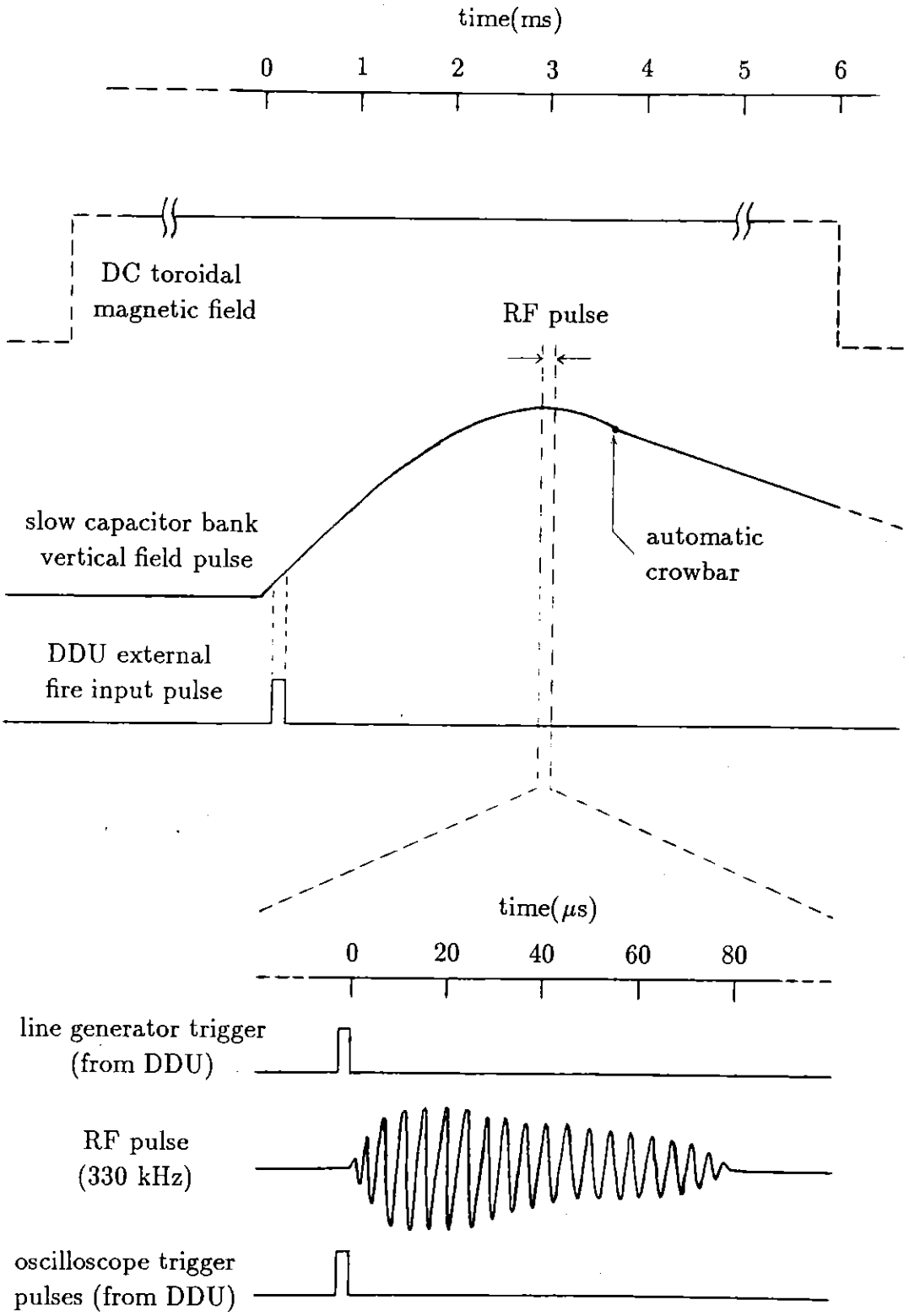

Figure 5.1 The discharge timing sequence.

attributed to an influx of particles which had adhered to the wall of the vacuum vessel during the period of inactivity. A succession of cleaning shots was sufficient to remove their influence.

5.3 The RF Magnetic Field

Ideally, the RF coil currents should be of equal amplitude and dephased by 90^0, so as to produce a circularly polarised travelling magnetic field. In practice, this ideal situation was not achieved.

A phase difference of approximately 90^0 was maintained for the entire duration of the discharge, in all experiments except the initial studies using $m = 0$ coils. In the $m = 0$ experiments, mutual coupling between the line generator loads caused the phase difference between the coil currents to decrease with time during the shot. In some extreme cases the phase difference reduced to zero or even changed sign during the discharge. In the latter case, the direction of the driven toroidal current was observed to change sign at the same time that the RF phasing became zero. Phase reversal and the accompanying change in the direction of the driven current, was also observed if one or both of the line generator loads were very badly tuned.

Careful monitoring of the pressure in the line generator spark gap switches was necessary to obtain a large percentage of acceptable shots for which the phase difference between the two RF sources was close to 90^0. Cleaning of the spark gap switches was required approximately every 1000 shots, because erosion of the electrodes caused unreliable timing and therefore bad relative phasing between the generator currents.

Typical line generator waveforms in the presence of an argon plasma are shown in Figure 5.2. It is clear that in each of the three devices, the amplitudes of the RF currents are unequal and decrease with time. Table 5.1 shows the peak amplitudes of the RF currents in Phase 1 and Phase 2, measured $\sim 15\mu s$ after the start of the pulse. The current amplitudes given in Table 5.1 differ by about 13% in Rythmac-1,2

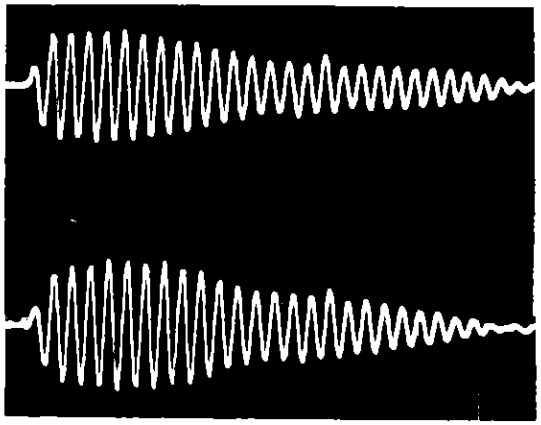

(a) Rythmac-1

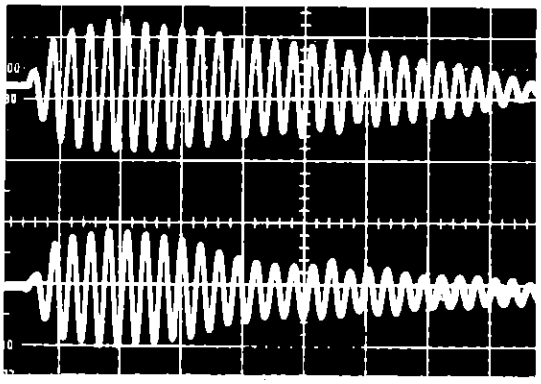

(b) Rythmac-2

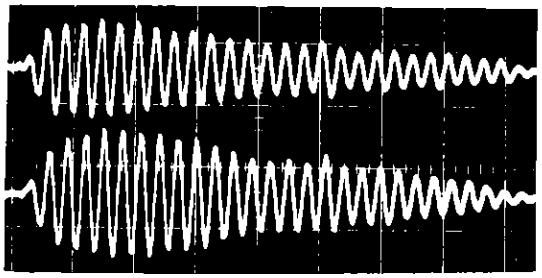

(c) Rythmac-3

Figure 5.2 Typical RF line generator current waveforms obtained with the helical coil structures in each of the three Rythmac devices. The timescale is $10\mu s$/div. The vertical scale is 1.67 kA/div. in each case.

Device	RF coil radius (cm)	RF coil current (Amps)			Average on-axis vacuum RF field $\bar{B}_\omega(G)$
		Phase 1 (I_1)	Phase 2 (I_2)	Average ($\bar{I}$)	
Rythmac-1	6.2	1470	1670	1570	73
Rythmac-2	7.0	1720	1520	1620	123
Rythmac-3	9.0	1230	1620	1420	33

Table 5.1: Amplitudes of the RF coil currents and average on-axis vacuum RF magnetic field at $t \simeq 15\mu$s derived from Figure 5.2

and by approximately 30% in Rythmac-3.

The vacuum amplitude of the applied RF magnetic field, B_ω, can be calculated from measurement of the RF coil geometry, line generator current amplitudes (I_1, I_2) and the relative phase between these two currents. Since the measured RF currents I_1 and I_2 are not equal, the applied RF field varies in amplitude during each cycle. The measured RF coil radii and the average amplitude of the currents through the coils, $\bar{I}$, as given in Table 5.1, are used in equation (2.23) to obtain the average on-axis RF field amplitude, $\bar{B}_\omega$ in each device. The results of these calculations, which assume that the phase difference between the two RF currents is 90^0, are also presented in Table 5.1. Note that the stated coil radius for the Rythmac-2 Helical Mesh Antenna is the average value of the coil radii for the *superposed* $m = +1$ and $m = -1$ coils.

The electron and ion cyclotron frequencies (for singly ionised argon) in the average RF field, $\bar{B}_\omega$, are given in Table 5.2. The condition $\omega_{ci} \ll \omega \ll \omega_{ce}$ (necessary for current drive) is seen to be satisfied in these experiments. It should be remembered that the vacuum RF field amplitude varies about the average value, $\bar{B}_\omega$, and that this average field amplitude decreases during the discharge; the values of the electron and ion cyclotron frequencies and the penetration of the RF field into the plasma vary accordingly.

Device	$\omega_{ci} = \frac{eB_\omega}{m_i}$ (rad/sec)	$\omega_{ce} = \frac{eB_\omega}{m_e}$ (rad/sec)	$\omega_{ci} : \omega : \omega_{ce}$ $\omega = 2\pi \times 330$ kHz
Rythmac-1	1.8×10^4	1.3×10^9	$(120)^{-1} : 1 : 620$
Rythmac-2	3.0×10^4	2.2×10^9	$(70)^{-1} : 1 : 1040$
Rythmac-3	8.0×10^3	5.8×10^8	$(260)^{-1} : 1 : 280$

Table 5.2: Ion and electron cyclotron frequencies in the average on-axis RF magnetic fields of the Rythmac devices.

5.4 m=0 RF Current Drive Experiments

For the initial experiments, an $m = 0$ coil structure spanning one quarter of a complete torus was wound on the 5/16 section of the Rythmac-1 vacuum vessel which is shown in Figure 3.4a. The periodicity length of the coil structure was $l = 20$cm. The Rogowski belt used to measure the quasi-steady driven toroidal current was located on the opposite side of the vacuum vessel. The slow capacitor bank described in Chapter 3 was used to produce a pulsed toroidal magnetic field of the order of 0.1 Tesla.

In the absence of an applied toroidal magnetic field, visible discharges were observed, in which the light output from the plasma was localised under the RF coil structure. Toroidal currents of several hundred Amperes were measured in these experiments. By performing several discharges with different gas filling pressures, the driven current was found to be optimised with $p \simeq 0.5$mTorr.

The application of an external toroidal magnetic field of approximately 0.1T was found to produce discharges in which the visible light output extended further around the torus, but was less intense. The presence of this relatively large toroidal field was found to substantially reduce the amount of driven toroidal current.

5.4.1 Dependence of the Driven Toroidal Current on the RF Coil Geometry.

All the experiments to be described in this section were performed in the absence of any externally imposed steady toroidal or vertical magnetic fields.

In an attempt to increase the magnitude of the driven toroidal current which was measured in the initial experiments, the periodicity length of the external coil structure was increased from $l = 20$cm to $l = 40$cm. The RF line generator frequency, f, was fixed. The phase velocity, $V_p = fl$, is thus increased by a factor of two in the new structure.

In the simple model of RF current drive, provided the amplitude and frequency of the external travelling RF field are appropriately chosen, the electrons can be regarded as being 'tied' to the magnetic field lines and it follows that the driven toroidal current is given by the expression:

$$I_{tor} = neV_pA \tag{5.1}$$

n is the electron number density, V_p is the phase velocity of the externally applied travelling RF field, and A is the cross sectional area of the discharge vessel.

Equation (5.1) indicates that, provided the electrons are fully entrained by the travelling RF field, an increase in the structure phase velocity, V_p, will give a corresponding increase in the driven toroidal current. However, in the experiments, it was observed that increasing the periodicity length of the RF coil structure in order to increase the phase velocity, did not result in larger values of measured driven current. Instead, several undesirable features and technical difficulties associated with the use of the $m = 0$ coil structures were discovered.

In the latter geometry, coupling between the RF coils and the toroidal field pancake coils resulted in sparking across some pancake coil connections, which presented serious technical dificulties. The RF coils were also found to exhibit strong mutual coupling which seriously degraded the line generator current waveforms. Equal am-

plitude RF current pulses with a phase difference of $\sim 90^0$ could not be obtained by simple tuning of the line generator loads. The phase difference between the two RF pulses was found to decrease with time, resulting in a lower value of driven plasma current. Coupling between the two RF phases was found to be present to varying degrees during all $m = 0$ current drive experiments described in this thesis.

The reduction in driven plasma current which was observed when the structure wavelength was increased from $l = 20$cm to $l = 40$cm may also be partly attributed to the resultant decrease in the strength of the r-component of the RF field, $\tilde{b}_r$. The amplitude of $\tilde{b}_r$ is important since in the $\langle \tilde{j} \times \tilde{b} \rangle$ model of $m = 0$ RF current drive, it is the $\langle \tilde{j}_{pol} \tilde{b}_r \rangle$ term in Ohm's law which provides the non-linear driving force in the toroidal direction.

Further attempts to increase the magnitude of the driven toroidal current were made using an $l = 20$cm, $m = 0$ coil structure in which the number of windings was increased so that the external structure covered a greater proportion of the vacuum vessel. The structure was expanded from 4 windings of 3 turns each, per phase, to 8 windings of 3 turns each, per phase. The current driven with the new coil structure was approximately twice the previously observed value. The number of turns in each winding was subsequently reduced from 3 to 2 in order to reduce the mutual coupling between the line generators and improve the quality of the RF current pulses.

Oscillograms of the line generator current waveforms for the latter RF coil geometry are shown in Figure 5.3. Note that the amplitudes of the line generator currents are not equal and that the relative phase between the two currents decreases markedly with time. The signal from the *unshielded* Rogowski belt used to measure the quasi-steady driven toroidal current, has a component at the line frequency (330kHz) which is present to varying degrees during all Rythmac discharges. This component is regarded as purely extraneous RF noise pick-up, but could in fact indicate modulation of the quasi-steady driven toroidal current resulting from large variations in the amplitude of the applied RF field during each cycle.

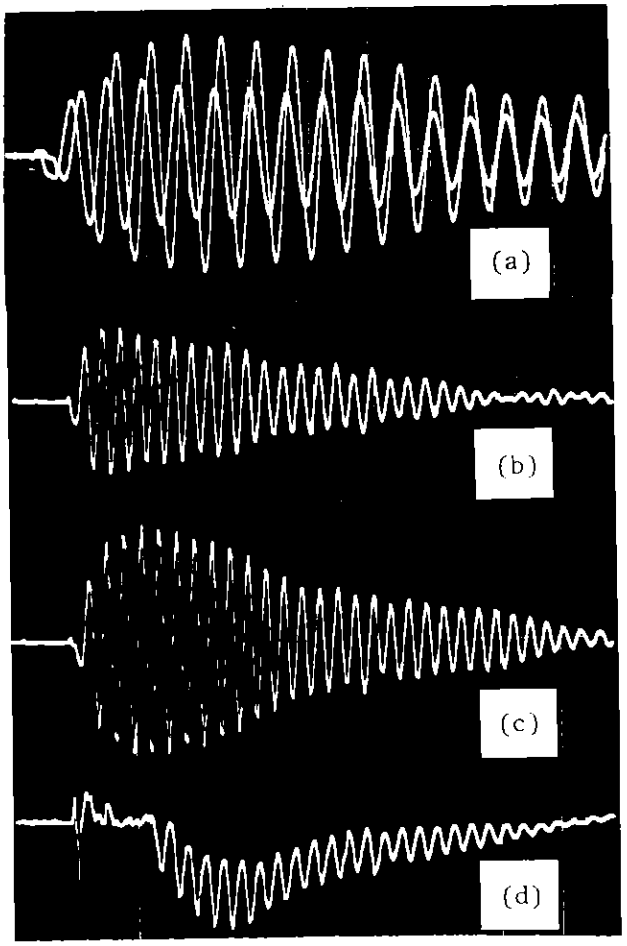

Figure 5.3 Oscillograms showing integrated Rogowski belt measurements of the line generator currents and the total toroidal current driven using an $m=0$ type coil structure. Each generator load consisted of 8 $m=0$ coils with 2 turns per coil. The periodicity length of the structure was $l=20$cm. (a) - Line generator current waveforms superposed and displayed on a timescale of 5μs/division to show the decrease in phase difference with time. (b) - Line generator 1 and (c) - Line generator 2 waveforms shown on a timescale of 10μs/division. The vertical scale in (a) - (c) is 0.67kA/division. Note that the amplitudes of the line generator currents are not equal. (d) - Rogowski belt measurement of the driven toroidal current. The timescale is 10μs/division. The vertical scale is 0.92kA/division. Experimental conditions: filling pressure=0.45mTorr Argon, line charging voltage=20kV, no external toroidal or vertical magnetic field.

5.4.2 Influence of the Steady Toroidal Magnetic Field on the Driven Toroidal Current

In this section, we present the results of studies conducted using the first $m = 0$ coil structure described in the previous section; $l = 20$cm, 4 windings each of 3 turns, per phase.

Experiments were conducted with a range of smaller externally applied DC toroidal magnetic fields, with field strengths up to a few hundred Gauss. The results of these experiments, using a filling pressure of 0.35mTorr argon, indicated the existence of an optimum external toroidal field for $m = 0$ RF current drive. An external vertical magnetic field was not used in these experiments.

The influence of the steady toroidal magnetic field on the time history of the driven plasma current can be seen in Figure 5.4. In Figure 5.5, we plot the peak value of the driven toroidal current for each value of the applied toroidal field in Figure 5.4. The optimum value of toroidal field is $\simeq$ 160G. The value of toroidal current measured with the optimum toroidal field applied is approximately twice the value observed in the absence of an external toroidal magnetic field.

5.5 m=1 Double Helix Current Drive Experiments

5.5.1 Dependence of the Driven Currents on the RF Field Strength $\bar{B}_\omega$.

Initial $m = 1$ double helix current drive plasma shots in Rythmac-1 were conducted with a line generator charging voltage of 20kV. However, in order to drive the largest possible plasma currents, a series of experiments was performed in which the line charging voltage was steadily increased from 20kV in steps of 1kV. Upon reaching 28kV, this value was adopted as an upper limit for the line charging voltage, since for voltages in excess of 28kV it became increasingly difficult to hold off the line

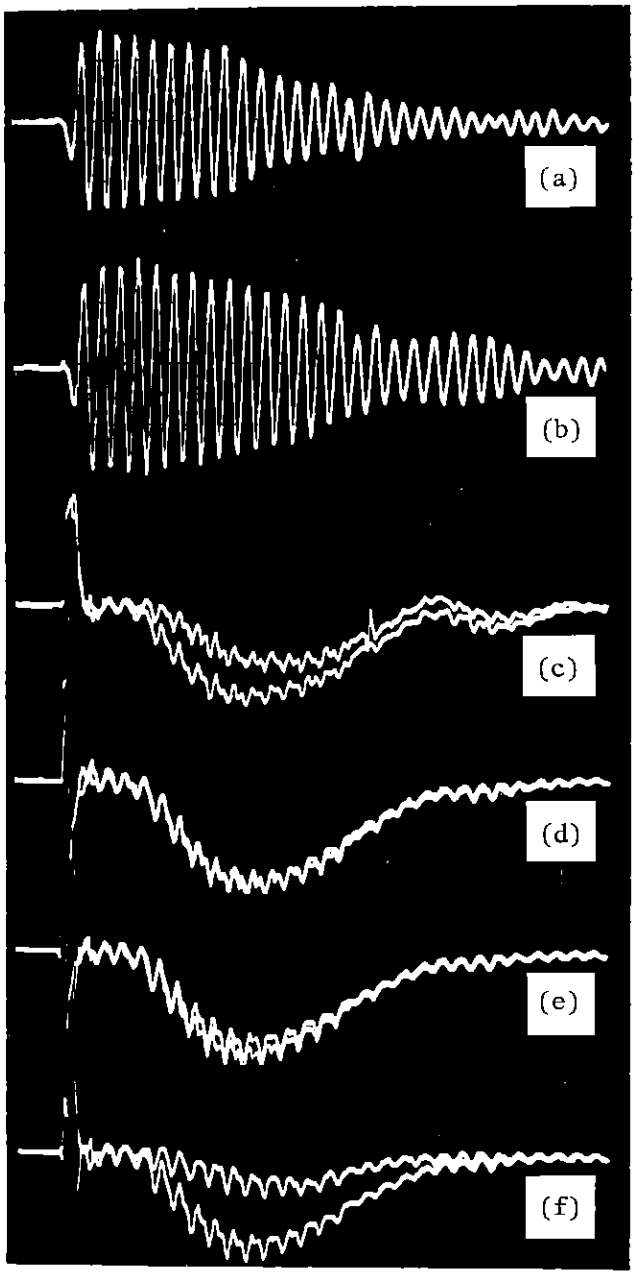

← Line 1

← Line 2

$B_{tor} = 0, 64^{*}$ G

$B_{tor} = 128, 192$ G

$B_{tor} = 192^{*}, 256$ G

$B_{tor} = 256^{*}, 320$ G

Figure 5.4 Oscillograms showing the influence of a steady toroidal magnetic field on the toroidal current driven using an $l = 20$cm, $m = 0$ coil structure. The antenna for these experiments consisted of 4 $m = 0$ coils of 3 turns each, per RF phase. The timescale in each oscillogram is 10μs/division. (a) - Line 1, (b) - Line 2 generator current waveforms. The vertical scale for both lines is 0.67kA/division. (c) - (f) Rogowski belt measurement of the driven toroidal current for each of the two indicated values of the steady applied toroidal field. The asterisks denote the field value of each pair for which the larger driven toroidal current was observed. Experimental conditions: filling pressure=0.35mTorr Argon, line charging voltage=20kV, no vertical field.

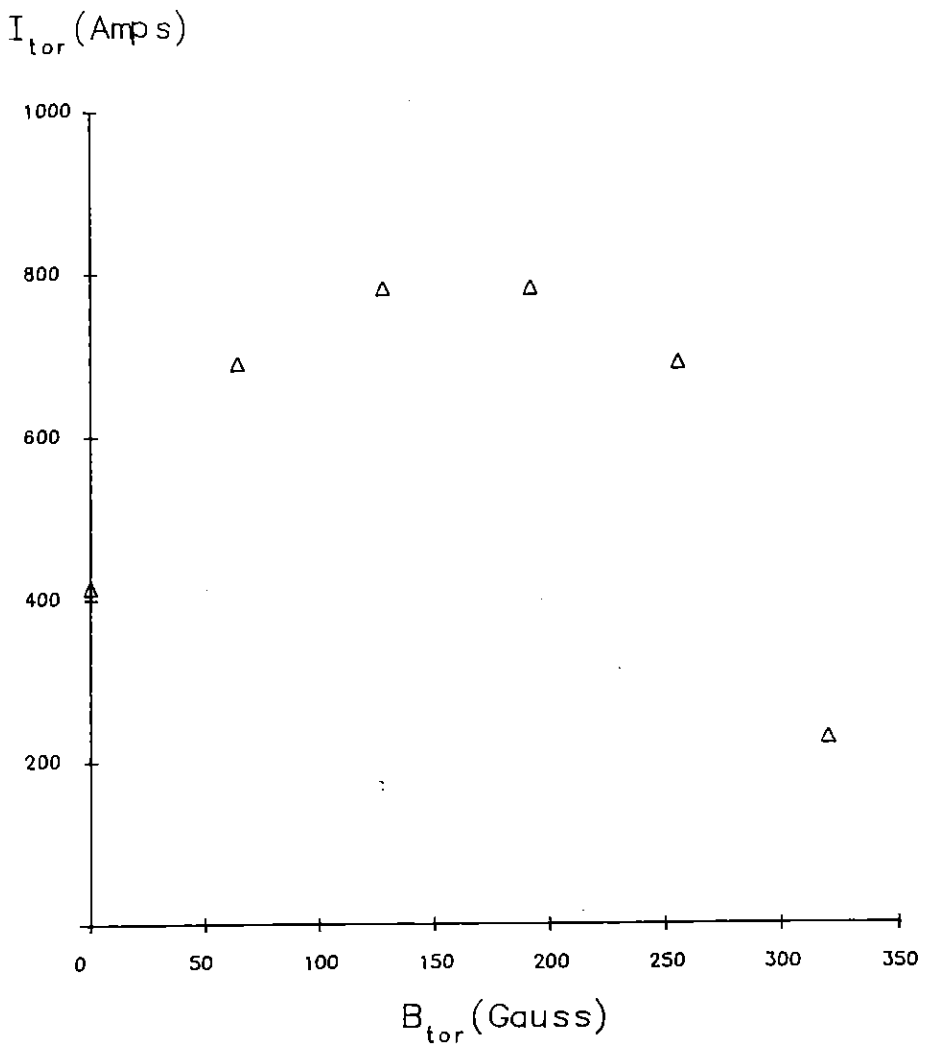

Figure 5.5 A plot constructed from the oscillogram data in Figure 5.4, showing the influence of the steady externally applied toroidal magnetic field on the peak quasi-steady toroidal current driven by the $m = 0$ coil structure. The value of the toroidal magnetic field on the minor axis ($r = R_0 = 25$cm) is given. The optimum value of toroidal field for current drive is $B_{tor} \simeq 160$G.

generator spark gap switches and prevent premature triggering of the lines. The possibility of damaging the line generators or the RF coils was also a serious concern at large voltages.

In Figure 5.6, we present oscillograms which show the dependence of the driven toroidal and poloidal plasma currents on the line generator charging voltage. Calibrated Rogowski belts (as described in Chapter 4) were used to measure the line generator currents and the quasi-steady toroidal current. The magnitude of the driven poloidal current is estimated from a measurement of $\Delta B_{tor}(R_0, 0)$, the change in the toroidal magnetic field at the minor axis.

A calibrated Hall probe was used to measure the quantity $\Delta B_{tor}(R_0, 0)$. The output of the Hall probe was filtered using a 40kHz RC lowpass filter of the type shown in Figure 4.3. The measured calibration constant for the filtered Hall probe signal was 2.37G/mV.

A DC toroidal magnetic field of 128G and a DC vertical magnetic field of 8G (both measured at $r = R_0$) were applied throughout these experiments. The secondary vertical field coil was absent in these experiments and the separation of the primary field coils was $d = 37$cm. The specifications for this vertical field coil geometry (which was one of several used in Rythmac-1) are listed in the first entry of Table 3.1. The filling gas pressure was 1mTorr of Argon.

The peak amplitudes of the RF coil currents (measured at $t \simeq 15\mu$s from the data presented in Figure 5.6) are used with equation (2.23) to calculate an average on-axis vacuum RF field strength, $\bar{B}_\omega$, for each value of the line charging voltage. The peak values of the toroidal and poloidal currents calculated from the data in Figure 5.6 are presented in Table 5.3 and plotted as a function of $\bar{B}_\omega$ in Figure 5.7. The non-linear dependence of the driven plasma currents on the strength of the applied RF field is clearly seen.

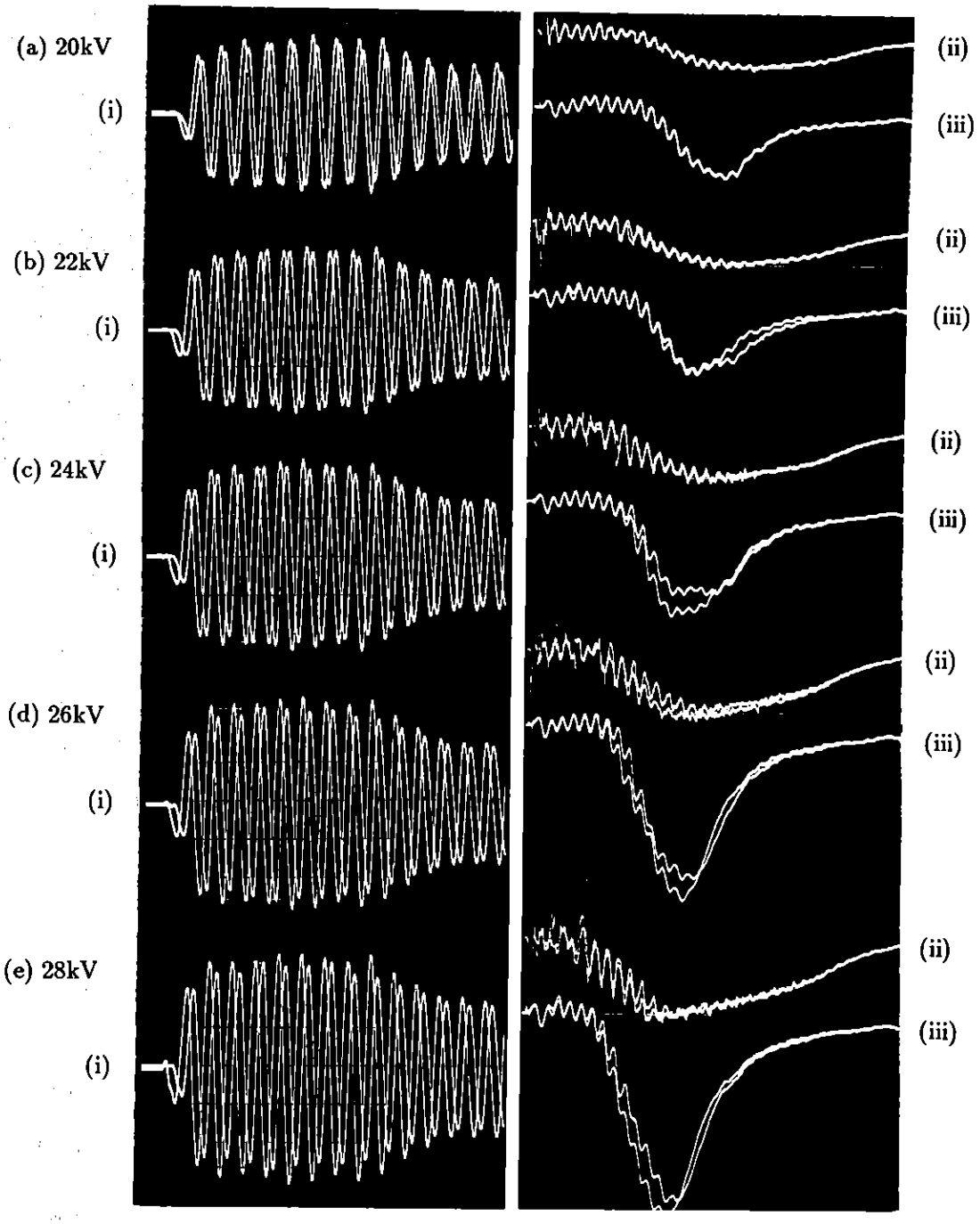

Figure 5.6 Oscillograms illustrating the dependence of the quasi-steady driven plasma currents on the line generator charging voltage. (i) Line generator current waveforms for the indicated line charging voltages. The current in Phase 1 is the larger of the two superposed RF currents in each of (a) - (e). The timescale is 5μs/div. and the vertical scale is 667Amps/div. (ii) Rogowski belt measurements of the driven toroidal current. The vertical scale in each of (a) - (e) is 460Amps/div. (iii) Calibrated Hall probe measurements of the change in the steady toroidal magnetic field on the minor axis, $\Delta B_{tor}(R_0, 0)$, produced by the quasi-steady driven poloidal current. The vertical scale is 47G /div. The timescale in each of (ii) and (iii) is 10μs/div. The experiments were performed in Argon at a pressure of 1 mTorr. A steady toroidal magnetic field of 128G and a DC vertical magnetic field of 8G (each measured at r=R_0) were applied.

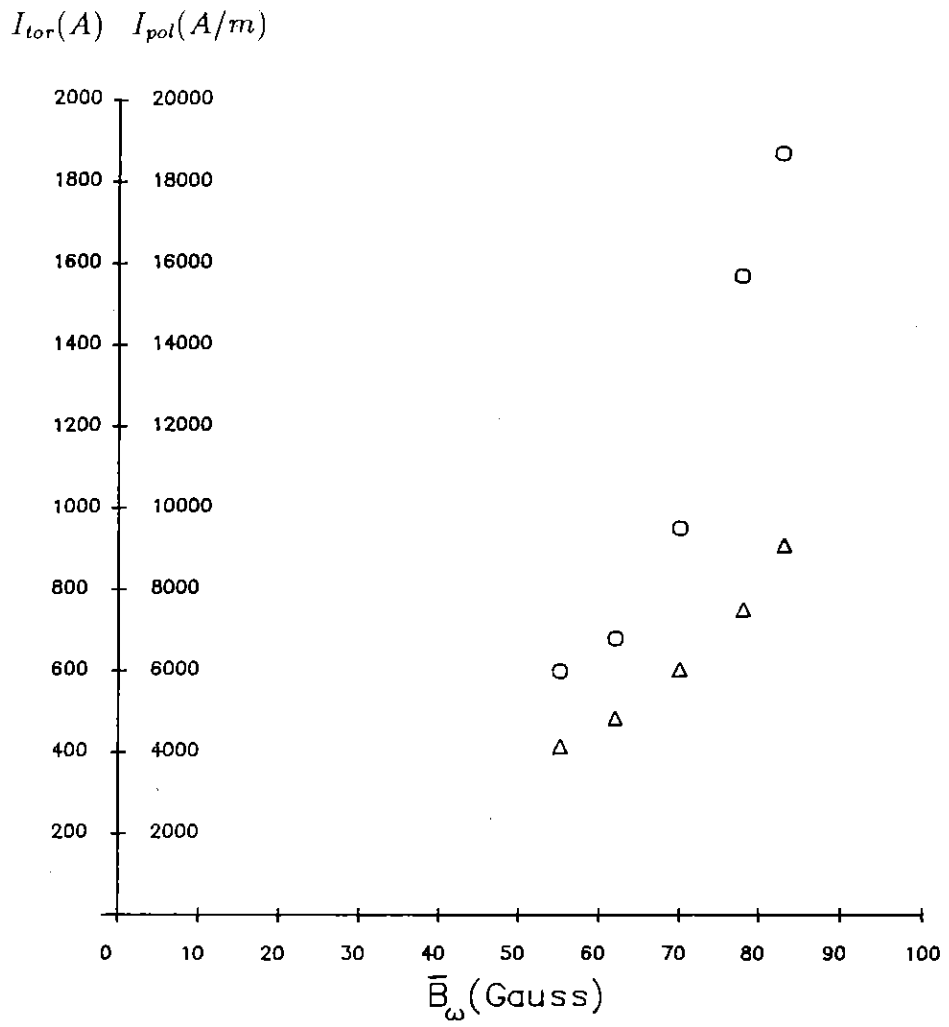

Figure 5.7 Peak values of the driven quasi-steady toroidal ($\triangle$) and poloidal ($\bigcirc$) plasma currents as a function of the average on-axis vacuum RF magnetic field strength (measured at $t \simeq 15\mu s$). The driven currents are obtained from the data in Figure 5.6 and are tabulated in Table 5.3. Note the non-linear dependence on the applied RF field strength.

Charging Voltage (kV)	RF current amplitude $\bar{I}$(Amps)	On-Axis RF field $\bar{B}_\omega$(G)	Toroidal Current I_{tor}(Amps)	$\Delta B_{tor}(R_0, 0)$ (G)	Poloidal Current I_{pol}(A/m)
20	1180	55	420	76	6000
22	1320	62	480	85	6800
24	1490	70	600	120	9500
26	1670	78	750	200	15700
28	1780	83	910	235	18700

Table 5.3: Magnetic fields and driven currents in Rythmac-1 for various line generator charging voltages.

5.5.2 Influence of Filling Pressure and External Fields on the Driven Plasma Current.

A set of exploratory experiments were performed in Rythmac-1 in order to determine the dependence of the driven toroidal plasma current on the experimental parameters: p (gas filling pressure), B_v (steady applied vertical magnetic field) and B_{tor} (steady applied toroidal magnetic field). From the results of these experiments, particular plasma/field configurations would be selected, in which to perform more detailed studies. The most physically interesting plasmas were deemed to be those in which the driven toroidal plasma current was largest for the longest period of time.

The total toroidal plasma current, $I_{tor}(t)$, was measured as a function of the external toroidal and vertical magnetic field strengths (at r=R_0,z=0) for several argon gas filling pressures. The specifications for the vertical field coils used in these experiments are listed in the first entry of Table 3.1.

Figure 5.8 shows $I_{tor}(t)$ for a range of B_{tor} and B_v values, obtained with a gas filling pressure of 1.0mTorr. In Figures 5.9, 5.10 and 5.11, we present the results obtained

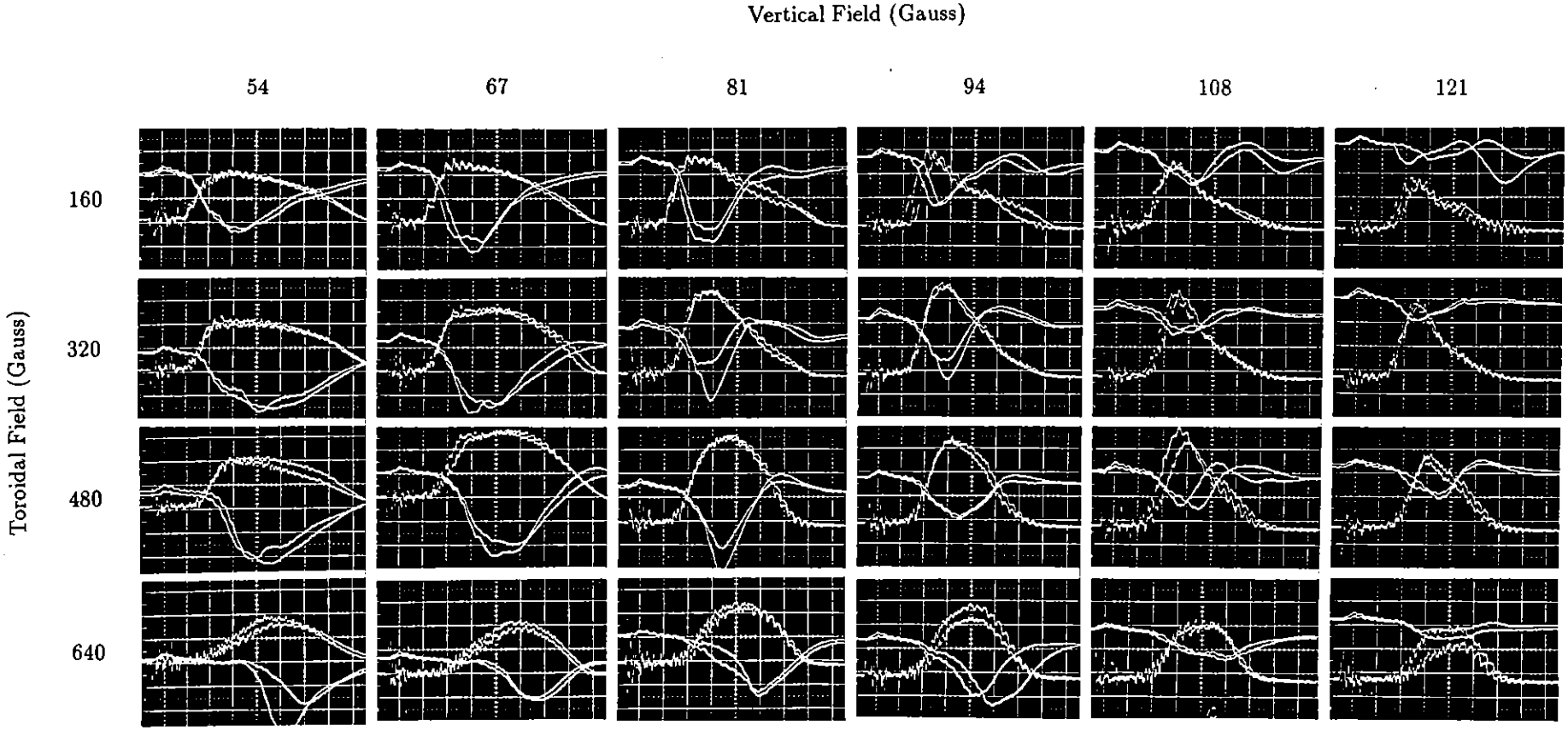

Figure 5.8 Time behaviour of I_{tor} and the associated B_{pol} (measured at $r = R_0, z = 0$) as a function of the applied toroidal and vertical magnetic field strengths. Two plasma shots are shown for each set of experimental conditions. Filling pressure: 1.0mTorr of Argon. Vertical scale: 461A/division (I_{tor}), 31G /division (B_{pol}). Horizontal scale: 10μs/division.

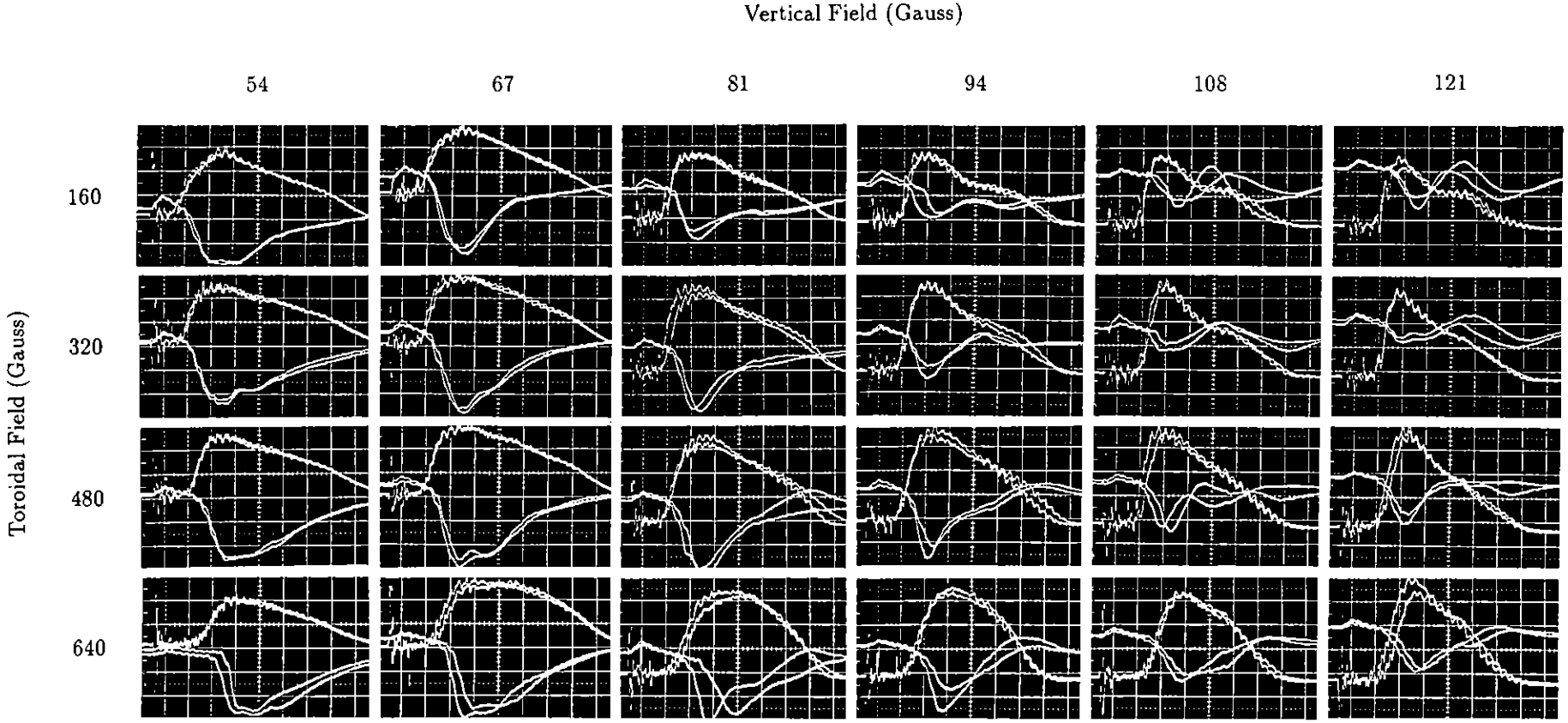

Figure 5.9 Caption reads as for Figure 5.8 except that filling pressure = 1.45mTorr of Argon.

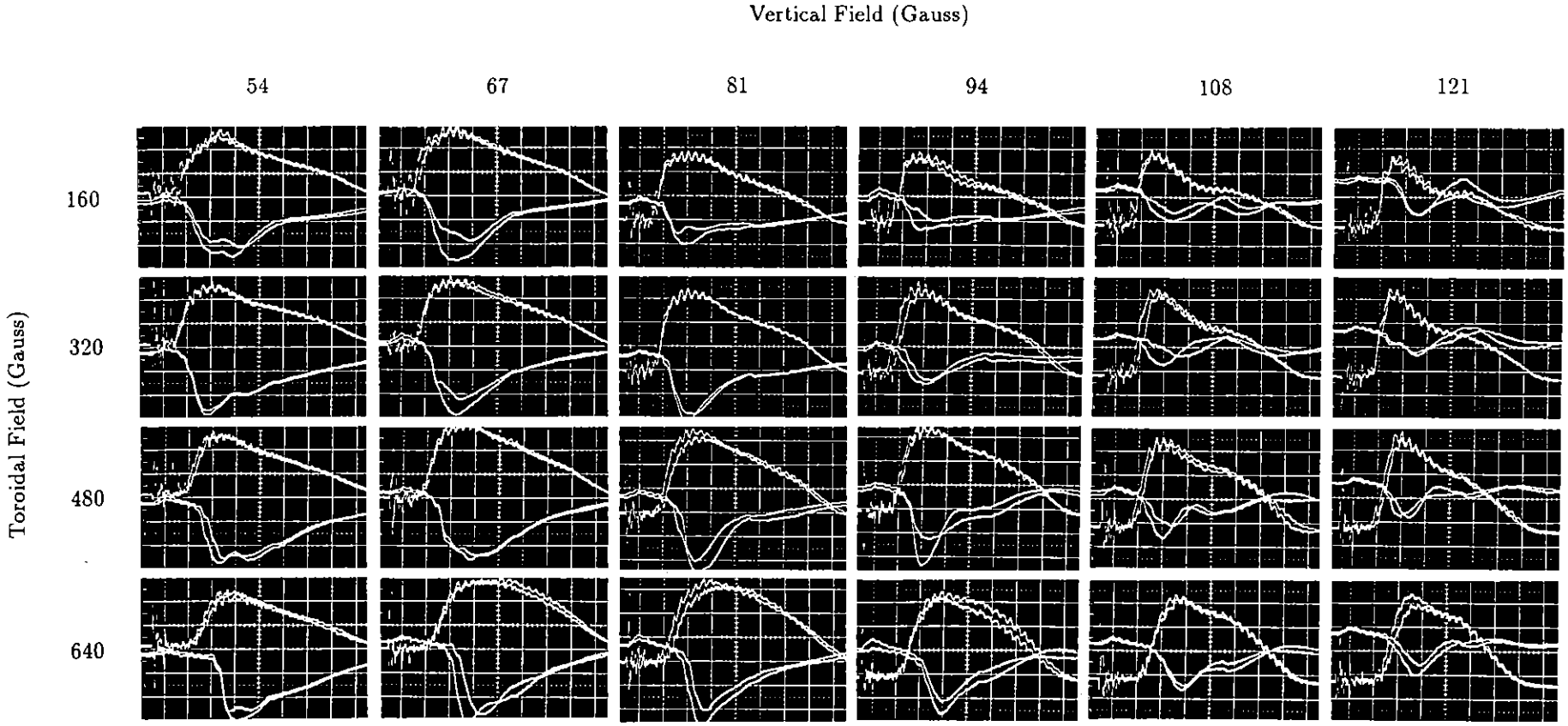

Figure 5.10 Caption reads as for Figure 5.8 except that filling pressure = 2.0mTorr of Argon.

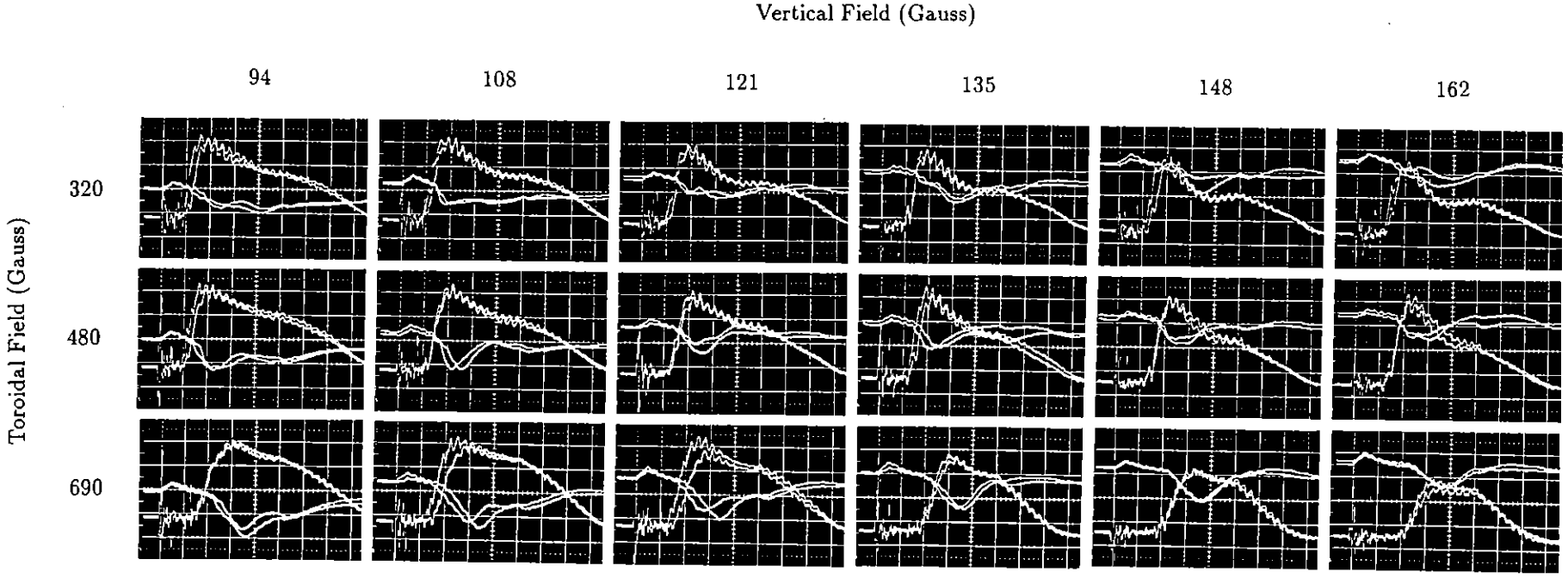

Figure 5.11 Caption reads as for Figure 5.8 except that filling pressure = 3.0mTorr of Argon.

with argon gas filling pressures of 1.45mTorr, 2.0mTorr and 3.0mTorr respectively.

In order to assess the reproducibility of the discharges, two plasma shots were recorded for each set of experimental conditions shown in Figures 5.8 to Figure 5.11 inclusive. The second trace in each of the oscillograms is the output of a small wirewound B_z probe located at the centre of the minor section (r=R_0,z=0). The probe signal was conditioned as shown in Figure 4.1 and used to detect the position and movement of the toroidal plasma current in the major radial direction. If the centroid of the toroidal current distribution is located on the minor axis, the probe signal is expected to vanish.

5.6 m=+and−1 Helical Mesh Current Drive Experiments

The experiments were conducted in the Rythmac-2 device using the $m = +and -1$ helical mesh antenna which is shown schematically in Figure 3.9.

By making different connections, the helical mesh antenna could also be operated as just an $m = +1$ or just an $m = -1$ double helix antenna. The impedance presented to each of the RF sources differs in the different coil configurations, but the operating conditions (*viz* line charging voltages) were chosen so that for the data presented in this section, the magnitudes of the RF currents in the antenna windings were approximately the same.

The data presented compares the results for the driven toroidal and poloidal current from the three different antenna configurations; $m = +1$ double helix in Figure 5.12a, $m = -1$ double helix in Figure 5.12b and the $m = +and - 1$ helical mesh antenna in Figure 5.12c. The toroidal current was measured with a calibrated Rogowski belt. The poloidal current was monitored by using an integrated wirewound probe placed at the centre of the minor section to measure the change in the toroidal field, $\Delta B_{tor}(R_0, 0)$.

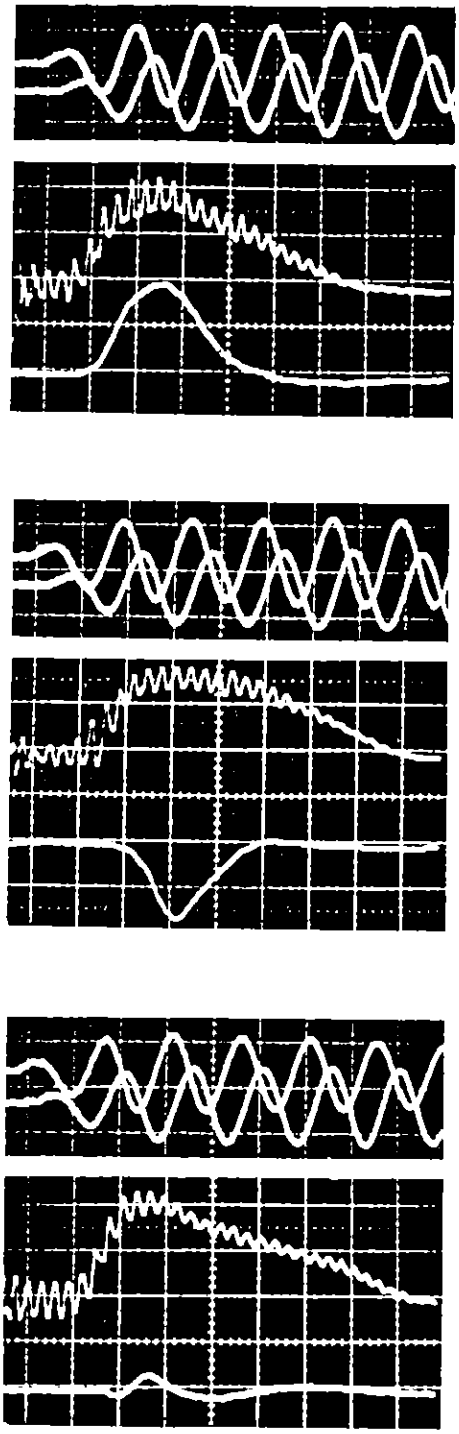

Figure 5.12 Oscillogram data for the (a) $m = +1$ double helix antenna, (b) $m = -1$ double helix antenna and (c) $m = +and - 1$ helical mesh antenna. (i) Line generator waveforms recorded at 2μs/div. to show the one quarter period time delay between the two phases. The vertical scale is 1.67kA/div. (ii) Quasi-steady driven toroidal current, I_{tor}, recorded at 10μs/div. The vertical scale is 430A/div. (iii) Change in the toroidal magnetic field on the minor axis, $\Delta B_{tor}(R_0, 0)$, caused by the driven poloidal current. The vertical scale is 31G /div. Experimental conditions: $p \simeq$ 1mTorr, $B_{tor} = 160$G , $B_v = 43$G.

For each case, the RF current waveforms in the two phases of the antennas are displayed to show the approximately equal magnitudes of current. The timescale is expanded compared to the driven current timescale, so that the time difference of one quarter of a period can be seen.

For all three cases the sign of the toroidal current is the same; that driven by the helical mesh antenna is slightly greater in magnitude. The $\Delta B_{tor}(R_0, 0)$ caused by the poloidal current driven with the $m = -1$ double helix antenna is opposite in sign to that for the $m = +1$ case, indicating that the poloidal currents flow in opposite directions for these two configurations. The helical mesh antenna makes a much smaller $\Delta B_{tor}(R_0, 0)$ consistent with a small driven poloidal current relative to that for the other two antennas.

5.7 The Quasi-steady Magnetic Field Structure of Rythmac Discharges.

In this section we present the results of a series of studies concerning the detailed quasi-steady magnetic field structure of selected discharges produced in each of the three Rythmac devices. The aim of these studies was to determine the influence of various parameters on the observed magnetic field structure. These parameters included the type of external RF coil structure used and the strength of the applied toroidal and vertical magnetic fields.

Other closely related studies included an experiment to determine whether the observed asymmetry of the field structure within the discharge vessel was local or global. The Rythmac-3 device was used to investigate the magnetic field structure at two distinct toroidal locations under the same discharge conditions. The field structure produced by a double helix antenna wound on only one half of the vacuum vessel was also investigated.

The magnetic field structure of each selected discharge was investigated by measur-

ing the major radial ($B_r(r,z)$) and vertical ($B_z(r,z)$) components of the quasi-steady magnetic field produced by the driven toroidal plasma current. In a small number of the selected discharges, the change in the toroidal component of the magnetic field, ($\Delta B_{tor}(r,z)$), associated with the driven poloidal current was also measured.

The detailed magnetic field measurements were made with a wirewound probe described in Section 4.2. This probe enabled measurements of two magnetic field components to be made at the same time. The probe was successively inserted into each of the retractable, re-entrant probe guides and data collected at a matrix of uniformly spaced r and z positions.

The conditioned (see Figure 4.1) raw probe data was sampled by a digital storage oscilloscope (256 samples with $\Delta t = 0.4\mu$s) and recorded onto flexible diskettes. It was not possible or even desirable to analyse the data at each of the 256 available timesteps. Instead, programs were written to condense the data, make adjustments for the probe calibration factor, and rewrite the results on disk in the form of an array of the measured quantity over r and z at twelve different timesteps, each separated by 8μs. The data in this form was transferred to the PRIME P750 mainframe computer for subsequent analysis.

On the timescale of the plasma discharge, the externally applied pulsed (or DC) vertical magnetic field is effectively constant and thus is not detected by the wirewound probe. It is therefore necessary to algebraically add to the experimental data, the components due to the external vertical field. The required $B_r^{vert}(r,z)$ and $B_z^{vert}(r,z)$ components were calculated at each point (r,z) of the measurement grid using analytic expressions for a single loop given by SMYTHE(1950). The contributions from each vertical field coil were calculated and summed using the specifications listed in Table 3.1.

The measurement of the magnetic field structure involved a large number of separate discharges. The satisfactory collation of magnetic field data, recorded in separate discharges into meaningful profiles requires a high degree of shot-to-shot reproducibil-

ity. Examples of the degree of reproducibility which could be obtained in the present experiments have already been presented in Figure 4.8, Figure 5.6 and Figures 5.8 - 5.11.

5.7.1 Major Radial and Vertical Magnetic Field Profiles.

Examples of the major radial and vertical profiles of the raw B_r and B_z data for a selected discharge in Rythmac-3 are shown in Figures 5.13 - 5.20. The profiles are constructed at two well separated times ($t_1 = 36\mu$s, $t_2 = 84\mu$s) during the discharge. Note that it is some 20μs into the shot before a significant amount of toroidal plasma current is driven.

The B_r and B_z data used to construct these profiles was collected on a 13×13 grid in the minor section, with a uniform spacing of $\Delta r = \Delta z = 1.0$cm. The working gas was argon at a filling pressure of 1.2mTorr. A DC toroidal field of 160G and a DC vertical field of 9.3G were applied.

5.7.2 Derivation of the Poloidal Flux Function and the Toroidal Current Density

The poloidal flux function is given by:

$$\Psi = \int \boldsymbol{B} \cdot \boldsymbol{dS}, \tag{5.2}$$

where the integration is performed over a surface spanning the centre of the toroid. For an axisymmetric toroidal plasma ($\partial/\partial\phi = 0$, where ϕ is the usual toroidal coordinate), all the field quantities are functions of the major radial (r) and vertical (z) coordinates only. For this situation, the magnetic field components can be expressed in terms of the poloidal flux function as follows:

$$B_r = \frac{-1}{2\pi r}\frac{\partial \Psi}{\partial z} \tag{5.3}$$

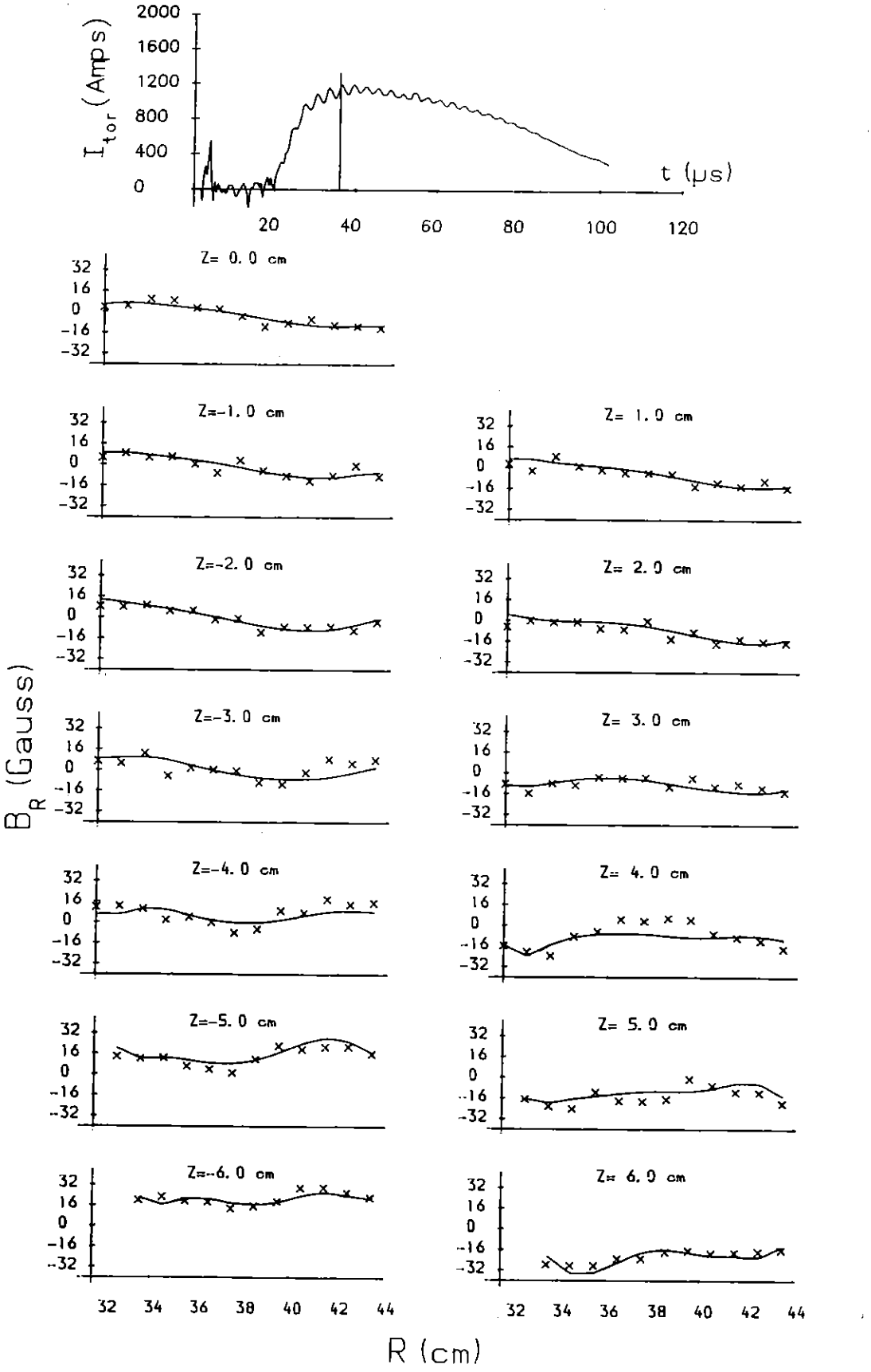

Figure 5.13 The experimentally measured distribution of the 'steady' major radial magnetic field component at $t = 36\mu$s. The solid curves in Figures 5.13 - 5.20 are obtained from a two-dimensional polynomial fit to the raw data.

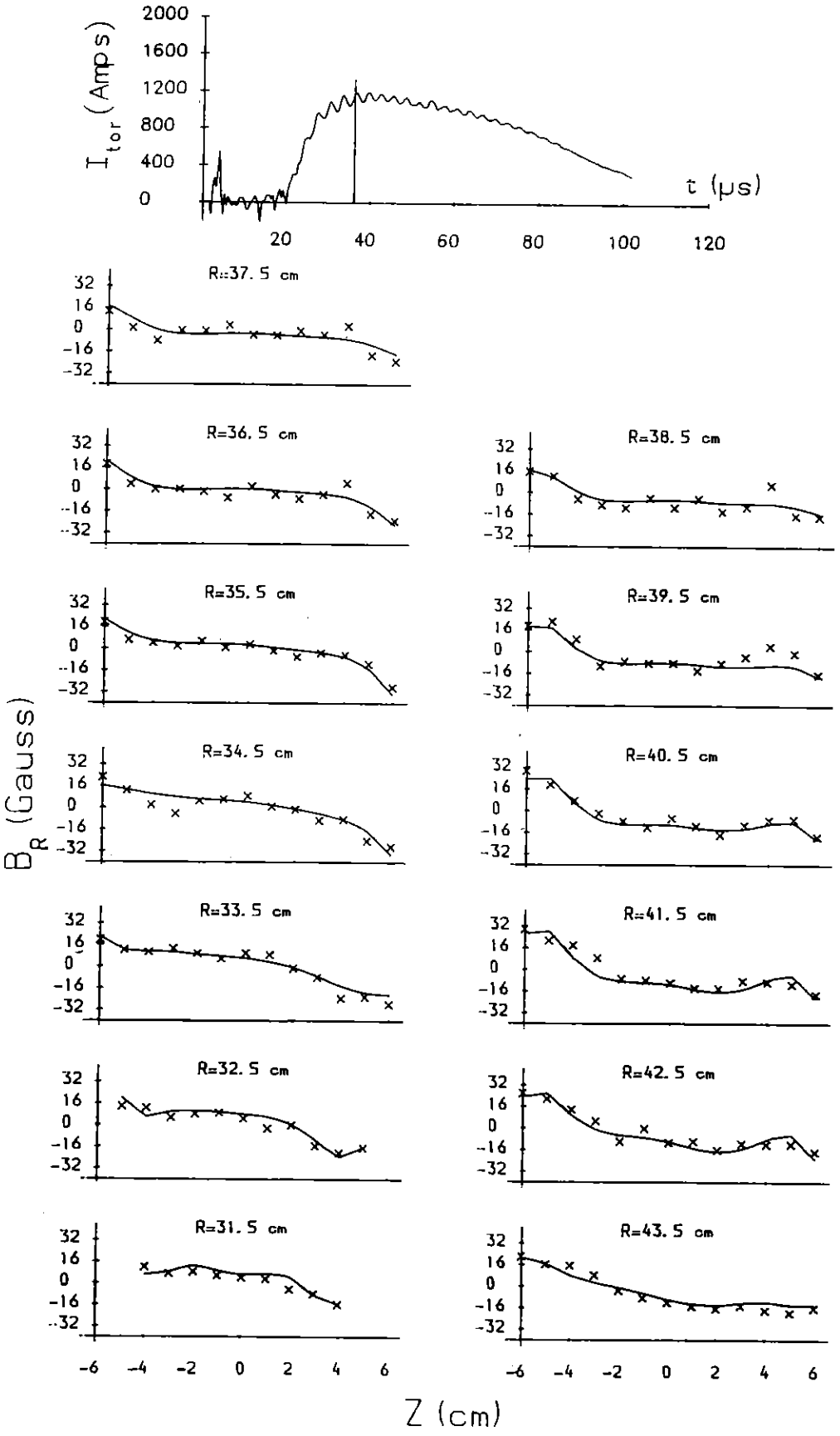

Figure 5.14 The distribution of the 'steady' major radial magnetic field component at $t = 36\mu s$.

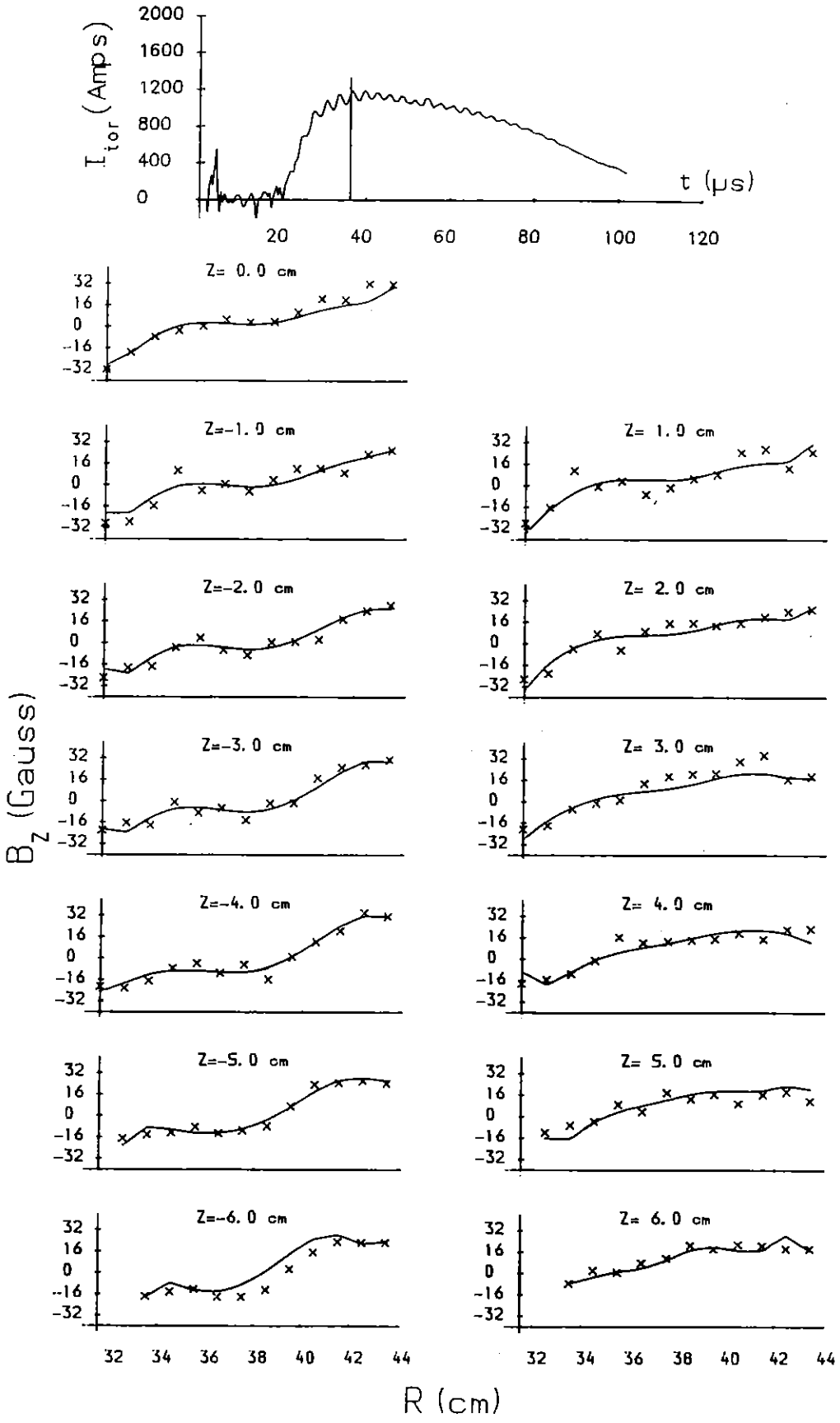

Figure 5.15 The distribution of the 'steady' vertical magnetic field component at $t = 36\mu$s.

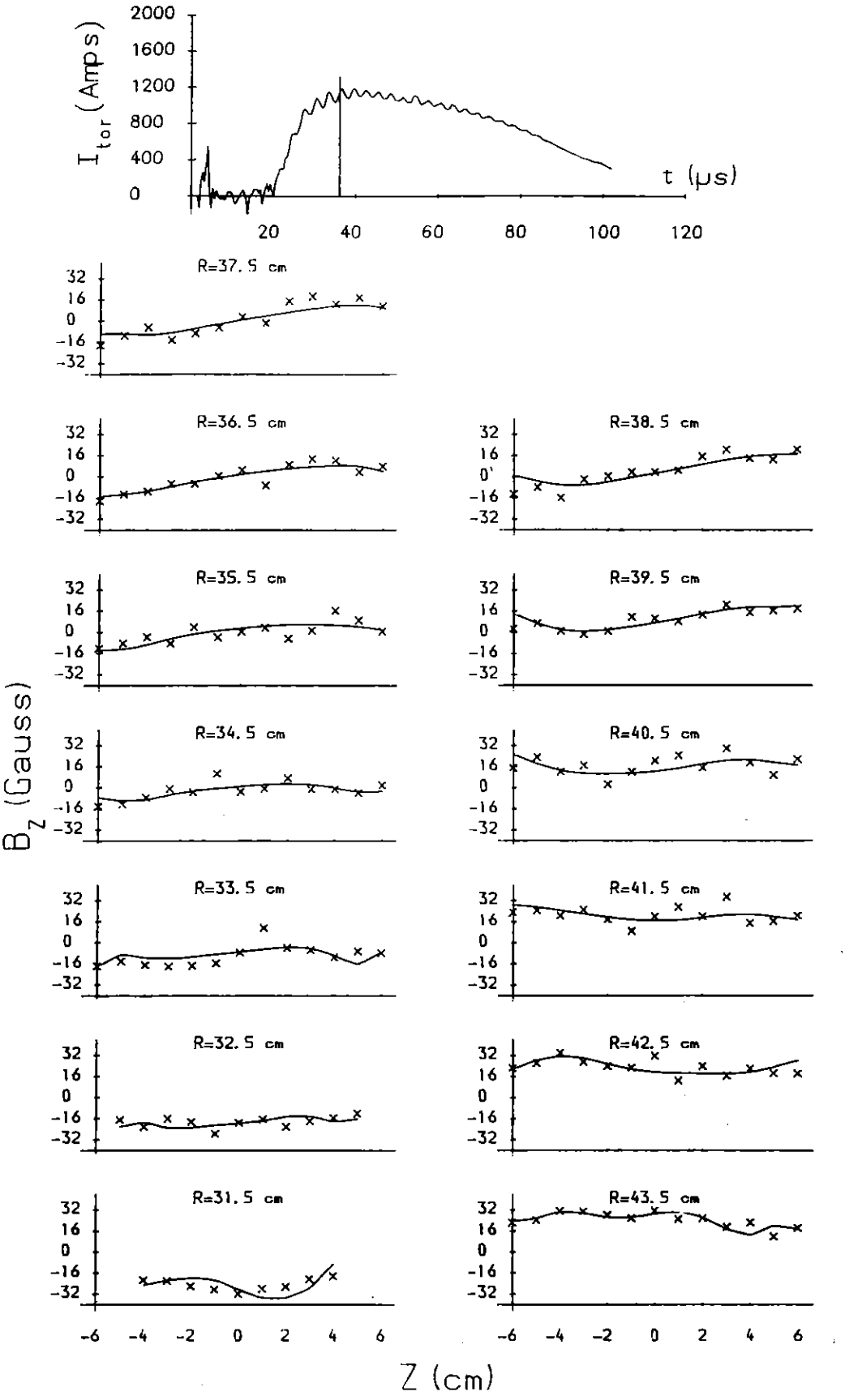

Figure 5.16 The distribution of the 'steady' vertical magnetic field component at $t = 36\mu$s.

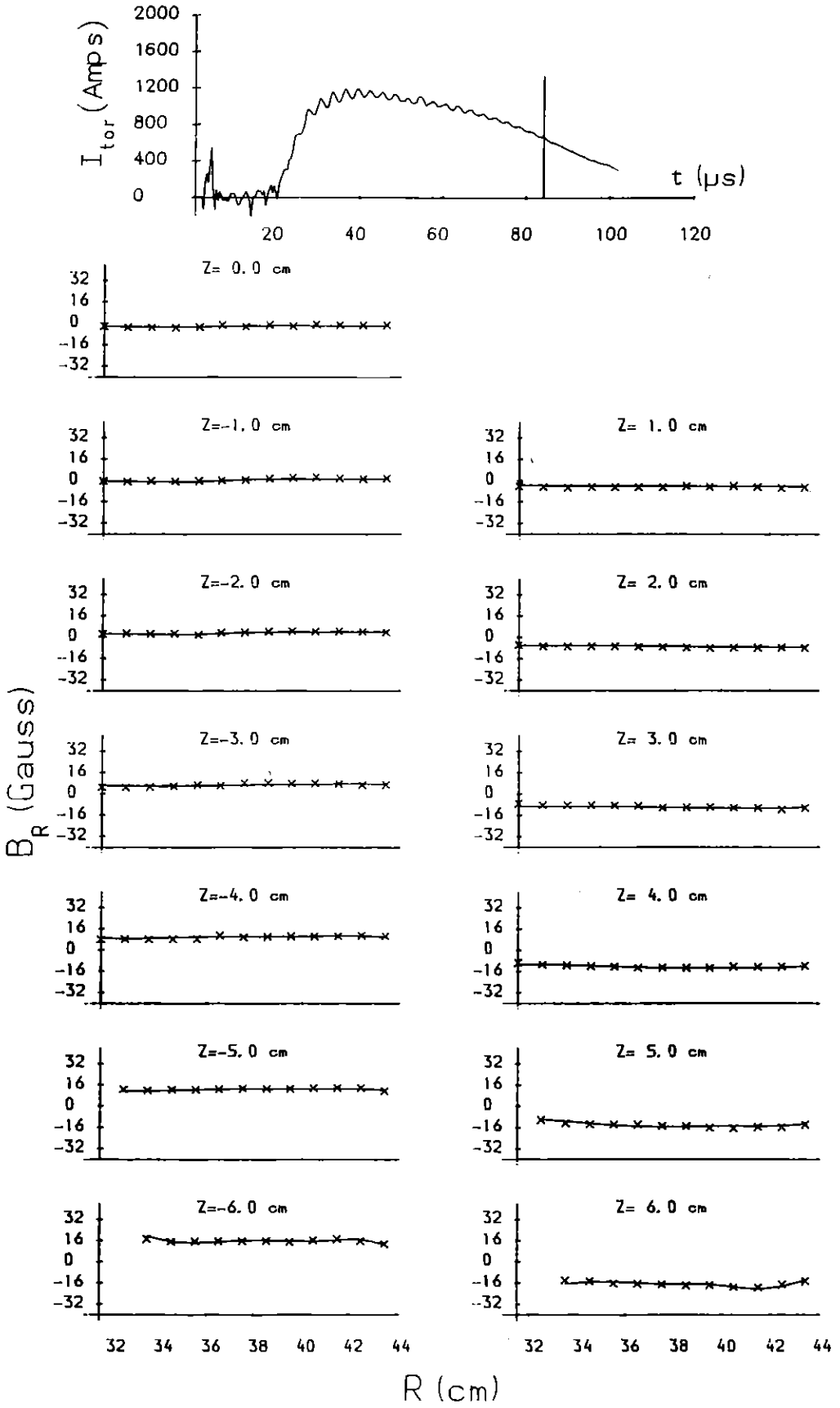

Figure 5.17 The distribution of the 'steady' major radial magnetic field component at $t = 84\mu$s.

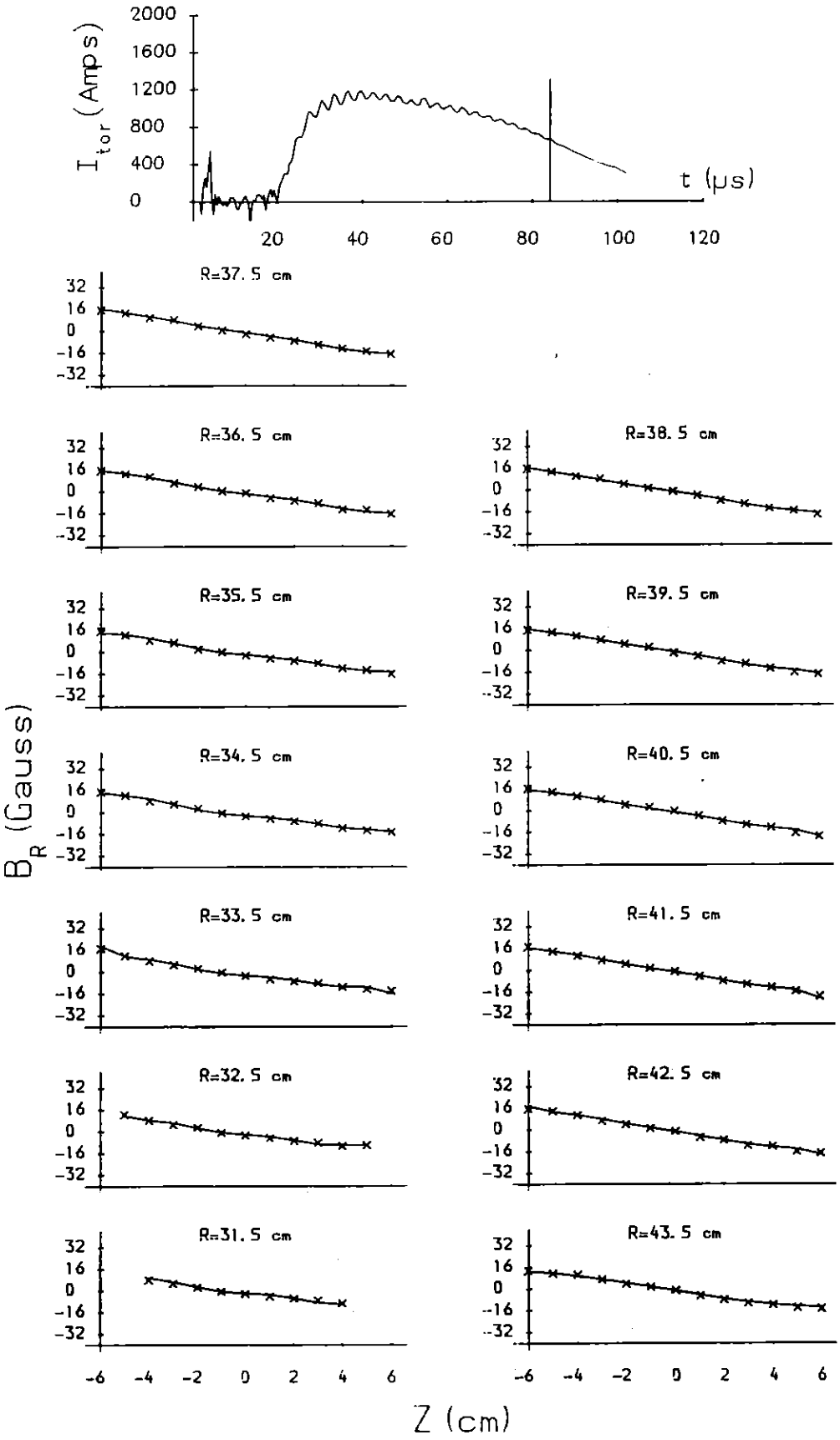

Figure 5.18 The distribution of the 'steady' major radial magnetic field component at $t = 84\mu$s.

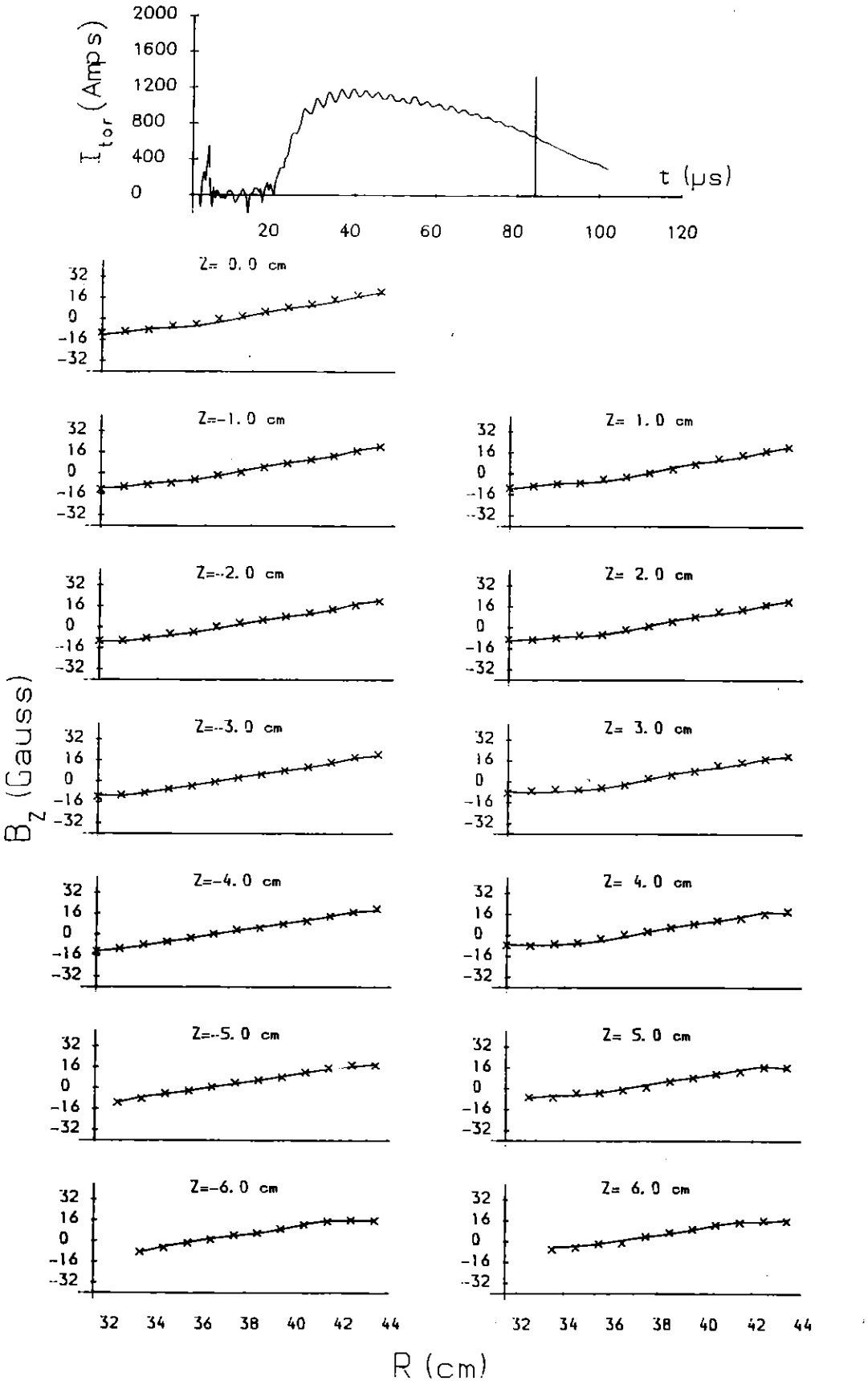

Figure 5.19 The distribution of the 'steady' vertical magnetic field component at $t = 84\mu$s.

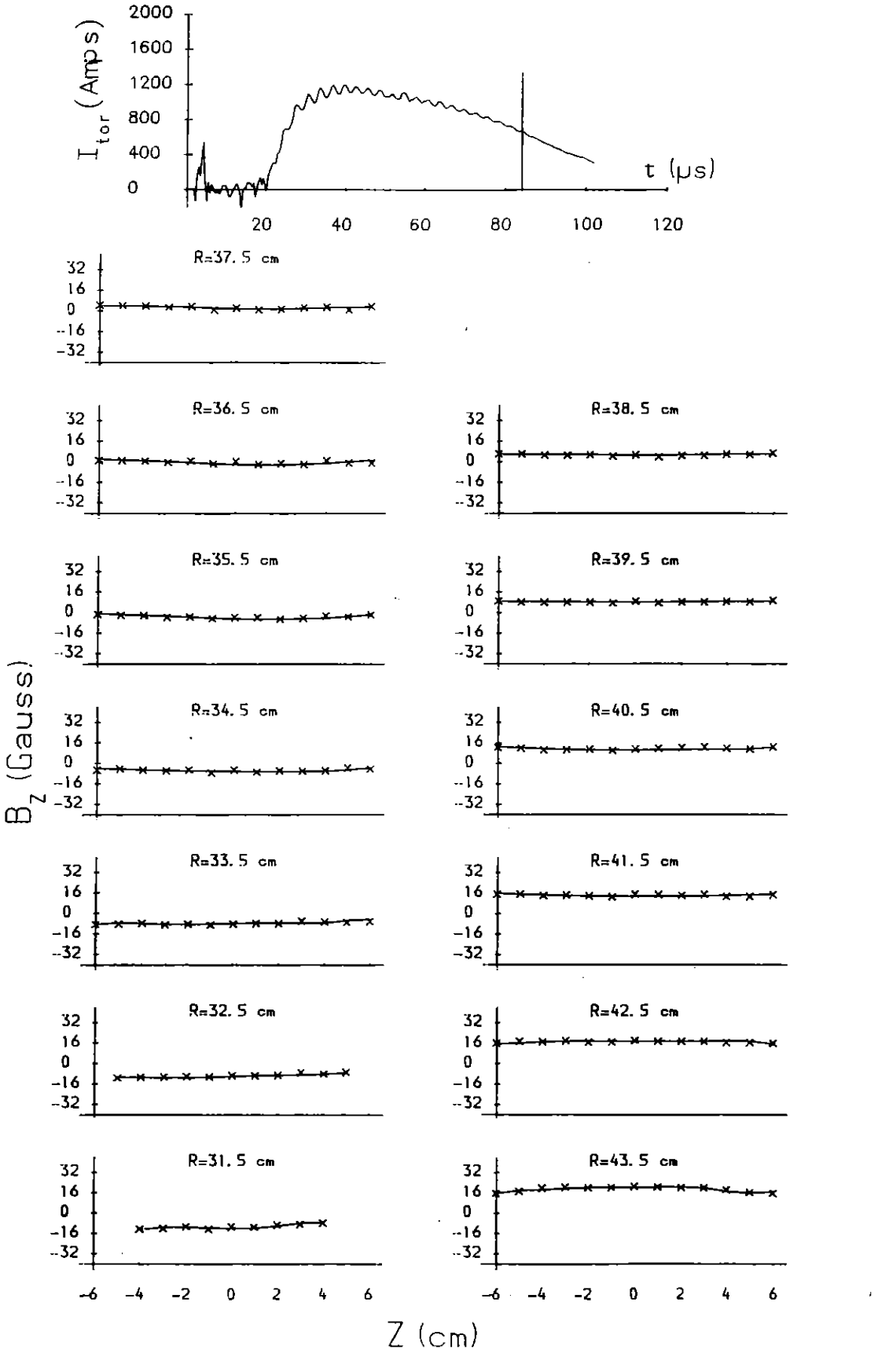

Figure 5.20 The distribution of the 'steady' vertical magnetic field component at $t = 84\mu$s.

$$B_z = \frac{1}{2\pi r}\frac{\partial \Psi}{\partial r} \tag{5.4}$$

$$B_{tor} = B_{tor}(r,z) \tag{5.5}$$

The toroidal current density is given in terms of the magnetic field components:

$$\mu_0 J_{tor} = \frac{\partial B_r}{\partial z} - \frac{\partial B_z}{\partial r} \tag{5.6}$$

The poloidal flux and toroidal current density calculated numerically from the raw B_r and B_z probe data is subject to experimental errors in the data. The poloidal flux function is calculated by integrating the raw magnetic field data and so to some degree performs an automatic smoothing of the experimental errors. However, determination of the toroidal current density involves calculating spatial derivatives of the magnetic field, and it is well known that numerical differentiation of experimental data is extremely sensitive to small errors in the measurements.

For the reasons just outlined, it was decided to smooth the data by fitting two-dimensional polynomial surfaces (in r and z) to the raw magnetic probe data. We now give a brief description of the polynomial fitting algorithm.

The poloidal flux function Ψ can be represented by a two-dimensional polynomial of the general form:

$$\Psi = \sum_{\alpha=0}^{N_1}\sum_{\beta=0}^{N_2} a_{\alpha\beta}(r-R_0)^\alpha z^\beta, \tag{5.7}$$

where R_0 is the major radius and the coefficients $a_{\alpha\beta}$ have yet to be determined. The corresponding forms of the polynomials to be fitted to B_r and B_z are obtained by substituting the expression for the poloidal flux function (equation (5.7)) into equations (5.3) and (5.4). These polynomial fits to B_r and B_z ensure that the physical constraint $\nabla \cdot \boldsymbol{B} = 0$ is automatically satisfied. In the algorithm, polynomials were used to fit the quantities rB_r and rB_z rather than B_r and B_z respectively. The appropriate forms of the fitting polynomials are then:

$$rB_r(r,z) = -\frac{\partial \psi}{\partial z} = -\sum_{\alpha=0}^{N_1}\sum_{\beta=0}^{N_2}\left\{\beta a_{\alpha\beta}(r-R_0)^\alpha z^{\beta-1}\right\} \tag{5.8}$$

$$rB_z(r,z) = \frac{\partial \psi}{\partial r} = \sum_{\alpha=0}^{N_1}\sum_{\beta=0}^{N_2}\left\{\alpha a_{\alpha\beta}(r-R_0)^{\alpha-1}z^{\beta}\right\} \tag{5.9}$$

Where we have introduced the stream function ψ which is related to the poloidal flux by:

$$\psi = \frac{\Psi}{2\pi}$$

Suppose we have measurements of B_r and B_z over the array positions (r_i, z_j), $i = 1, \ldots N_r$, $j = 1, \ldots N_z$. We denote these data points by $\hat{B}_r(r_i, z_j)$ and $\hat{B}_z(r_i, z_j)$. We wish to fit two-dimensional polynomials with the forms given in equation (5.8) and equation (5.9) to these data points. The coefficients $a_{\alpha\beta}$ are to be determined from a least squares fit to the data, so that the sum of the squares of the residuals;

$$S = S_r + S_z = \sum_{i=1}^{N_r}\sum_{j=1}^{N_z}\left[r_i\hat{B}_r(r_i,z_j) + \sum_{\alpha=0}^{N_1}\sum_{\beta=0}^{N_2}\left\{\beta a_{\alpha\beta}(r_i-R_0)^{\alpha}z_j^{\beta-1}\right\}\right]^2$$
$$+ \sum_{i=1}^{N_r}\sum_{j=1}^{N_z}\left[r_i\hat{B}_z(r_i,z_j) - \sum_{\alpha=0}^{N_1}\sum_{\beta=0}^{N_2}\left\{\alpha a_{\alpha\beta}(r_i-R_0)^{\alpha-1}z_j^{\beta}\right\}\right]^2 \tag{5.10}$$

is a minimum. The condition for S to be a minimum is:

$$\frac{\partial S}{\partial a_{\epsilon\delta}} = 0 \qquad \text{for} \qquad (\epsilon = 0, 1, \ldots N_1 \text{ and } \delta = 0, 1, \ldots N_2) \tag{5.11}$$

i.e.

$$\sum_{i=1}^{N_r}\sum_{j=1}^{N_z}\left\{\left[r_i\hat{B}_r(r_i,z_j) + \sum_{\alpha=0}^{N_1}\sum_{\beta=0}^{N_2}\beta a_{\alpha\beta}(r_i-R_0)^{\alpha}z_j^{\beta-1}\right]\delta(r_i-R_0)^{\epsilon}z_j^{\delta-1}\right\}$$
$$-\sum_{i=1}^{N_r}\sum_{j=1}^{N_z}\left\{\left[r_i\hat{B}_z(r_i,z_j) - \sum_{\alpha=0}^{N_1}\sum_{\beta=0}^{N_2}\alpha a_{\alpha\beta}(r_i-R_0)^{\alpha-1}z_j^{\beta}\right]\epsilon(r_i-R_0)^{\epsilon-1}z_j^{\delta}\right\} = 0 \tag{5.12}$$

Equation (5.12) can be written in the form:

$$\sum_{\alpha=0}^{N_1}\sum_{\beta=0}^{N_2}T_{\epsilon\delta\alpha\beta}a_{\alpha\beta} = V_{\epsilon\delta}, \tag{5.13}$$

where the tensors are given by:

$$T_{\epsilon\delta\alpha\beta} = \sum_{i=1}^{N_r}\sum_{j=1}^{N_z}\left[\beta\delta(r_i-R_0)^{\alpha+\epsilon}z_j^{\beta+\delta-2} + \alpha\epsilon(r_i-R_0)^{\alpha+\epsilon+2}z_j^{\beta+\delta}\right] \tag{5.14}$$

$$V_{\epsilon\delta} = \sum_{i=1}^{N_r}\sum_{j=1}^{N_z}\left[r_i\hat{B}_z(r_i,z_j)\epsilon(r_i-R_0)^{\epsilon-1}z_j^{\delta} - r_i\hat{B}_r(r_i,z_j)\delta(r_i-R_0)^{\epsilon}z_j^{\delta-1}\right] \tag{5.15}$$

By performing the index mapping:

$$\begin{aligned} \nu &= \alpha(N_2+1)+\beta \\ \mu &= \epsilon(N_2+1)+\delta \end{aligned}$$

the tensor $T_{\epsilon\delta\alpha\beta}$ is reduced to a matrix $T_{\mu\nu}$ and the matrix $V_{\epsilon\delta}$ becomes a vector V_μ. Equation (5.13) then reduces to:

$$\sum_{\nu=0}^{N_1(N_2+1)+N_2} T_{\mu\nu}A_\nu = V_\mu \tag{5.16}$$

Equation (5.16) represents a set of $(N_1+1)\times(N_2+1)$ linear equations in the same number of unknowns A_ν. The double precision Harwell library subroutine MA21AD was used to solve equation (5.16) for the polynomial coefficients A_ν.

The calculation of the elements of the tensor $T_{\mu\nu}$ required a relatively large amount of computer time. However, as these elements depended only upon the coordinates of the mesh points (r_i, z_j) and not on the measured data, they were only calculated once for a given polynomial order (N_1, N_2) and measurement grid. The same tensor elements were used to calculate the polynomial coefficients $a_{\alpha\beta}$ at each of the twelve different timesteps.

The fitted form of the toroidal current density can be derived from equations (5.6), (5.8) and (5.9). We obtain:

$$\mu_0 J_{tor} = -\frac{1}{r_i^2}\sum_{\alpha=0}^{N_1}\sum_{\beta=0}^{N_2} a_{\alpha\beta}\left[\begin{array}{r} r_i\beta(\beta-1)(r_i-R_0)^\alpha z_j^{\beta-2} - \alpha(r_i-R_0)^{\alpha-1}z_j^\beta \\ +r_i\alpha(\alpha-1)(r_i-R_0)^{\alpha-2}z_j^\beta \end{array}\right] \tag{5.17}$$

Various polynomial orders were investigated in the fitting algorithm. At low orders, the polynomial failed to provide a reasonable fit to all the data points. At high orders, the polynomials would come close to the observed data, but exhibited large non-physical excursions in the regions between the points. Fitting with high order polynomials was also prohibitive as it required an excessive amount of computer time to calculate matrix elements and solve equation (5.16) for the polynomial coefficients.

The quality of the polynomial fit to the B_r and B_z magnetic field data was indicated by the error percentages, E_r and E_z, which express the sum of the residuals, S_r and S_z as a percentage of the rms value of the corresponding field component, as follows:

$$E_r = 100 \times \left[\frac{S_r}{\sum_{i=1}^{N_r} \sum_{j=1}^{N_z} \hat{B}_r^2(r_i, z_j)} \right]^{\frac{1}{2}} \tag{5.18}$$

$$E_z = 100 \times \left[\frac{S_z}{\sum_{i=1}^{N_r} \sum_{j=1}^{N_z} \hat{B}_z^2(r_i, z_j)} \right]^{\frac{1}{2}} \tag{5.19}$$

The curves shown in Figures 5.13 – 5.20 were obtained by fitting two-dimensional polynomials with $N_1 = 8, N_2 = 8$ to the raw data. These polynomial orders were generally used throughout the present work. The order of the polynomial fit in r and z was always chosen to be less than or equal to the corresponding number of measurement positions.

The polynomial fit to the raw data is seen to be much better at the later time ($84\mu s$) than at the earlier time ($36\mu s$). This observation is confirmed by the relative size of the error percentages for the fit at $84\mu s$ ($E_r = 7.7\%, E_z = 8.4\%$) and at $36\mu s$ ($E_r = 37.6\%, E_z = 32.6\%$) into the discharge. In these, and other poloidal flux magnetic field measurements, the polynomial fit to the data was found to improve markedly during the discharge. The relatively poor fit to the data at early times could be attributed to the lack of equilibrium during the 'start-up' phase and the breakdown of axisymmetry.

5.7.3 Poloidal Flux Contours.

The polynomial expression given in equation (5.7) can be used to calculate the poloidal flux at each of the mesh points to within an arbitrary constant and to produce poloidal flux contour plots. The unknown constant (a_{00}) reflects the fact that no information on the flux through the hole in the middle of the torus is available.

The value of this constant was chosen to obtain a maximum or minimum value of zero for the flux.

Poloidal flux contour plots were produced at each of the twelve different timesteps during the discharge by fitting the appropriate raw B_r and B_z data previously stored on flexible disk.

Fifteen sets of poloidal flux contour plots are presented. These data sets are the result of a wide range of studies performed in each of the three devices. The poloidal flux contour data sets are summarized in Table 5.4. N_r and N_z are the number of measurement positions in the major radial and vertical directions. N_1 and N_2 specify the order in r and z respectively of the two-dimensional polynomial used to fit the raw magnetic field data.

Contours of constant poloidal magnetic flux plotted in the minor section of the device are presented in Figures 5.21–5.35. The vessel wall is represented by a solid circle. Vertical lines through the driven toroidal current waveform are used as time markers to indicate each timestep during the discharge.

For a few of the experiments (Data Sets 12,14,15) we present contour plots of the driven toroidal current density calculated from the polynomial fitted B_r and B_z data. In some experiments (Data Sets 6,7), a wirewound magnetic probe was also used to make detailed measurements of the change in toroidal magnetic field associated with the driven poloidal current. The toroidal magnetic field measurements were fitted with a two-dimensional polynomial surface in order to smooth out experimental errors in the raw data. Contour plots of the raw data and the fitted polynomial surface are presented.

5.7.3.1 Effect of the Steady Toroidal Magnetic Field.

The first three sets of poloidal flux contours listed in Table 5.4 and shown in Figures 5.21, 5.22 and 5.23 were measured in order to study the effect of the steady

Data Set	Rythmac Device	Pressure (mTorr)	External Fields		Mesh		Poly. Order	
			B_{tor}(G)	B_v(G)	N_r	N_z	N_1	N_2
1	1	1.0	0	29	21	5	8	5
2	1	1.0	160	29	21	5	8	5
3	1	1.0	−160	29	21	5	8	5
4	1	1.0	160	44	21	5	8	5
5	1	1.0	−160	−44	21	5	8	5
6	1	1.0	160	36	21	5	8	5
7	2	2.0	−210	51	21	7	8	7
8	2	2.4	210	51	21	9	8	8
9	3	1.2	180	41	7	7	6	6
10	3	1.2	180	41	7	7	6	6
11	3	1.3	160	8.5	13	13	8	8
12	3	1.2	160	9.3	13	13	8	8
13	3	1.3	160	10.1	13	13	8	8
14	3	1.2	130	5.3	13	7	8	6
15	3	1.2	130	5.3	13	7	8	6

Table 5.4: Summary of Poloidal Flux Contour Data Sets. The $m = 1$ double-helix antenna was used in all experiments, except Data Sets 7,8 in Rythmac-2, where the external RF coil structure was the $m = +and- 1$ helical mesh antenna.

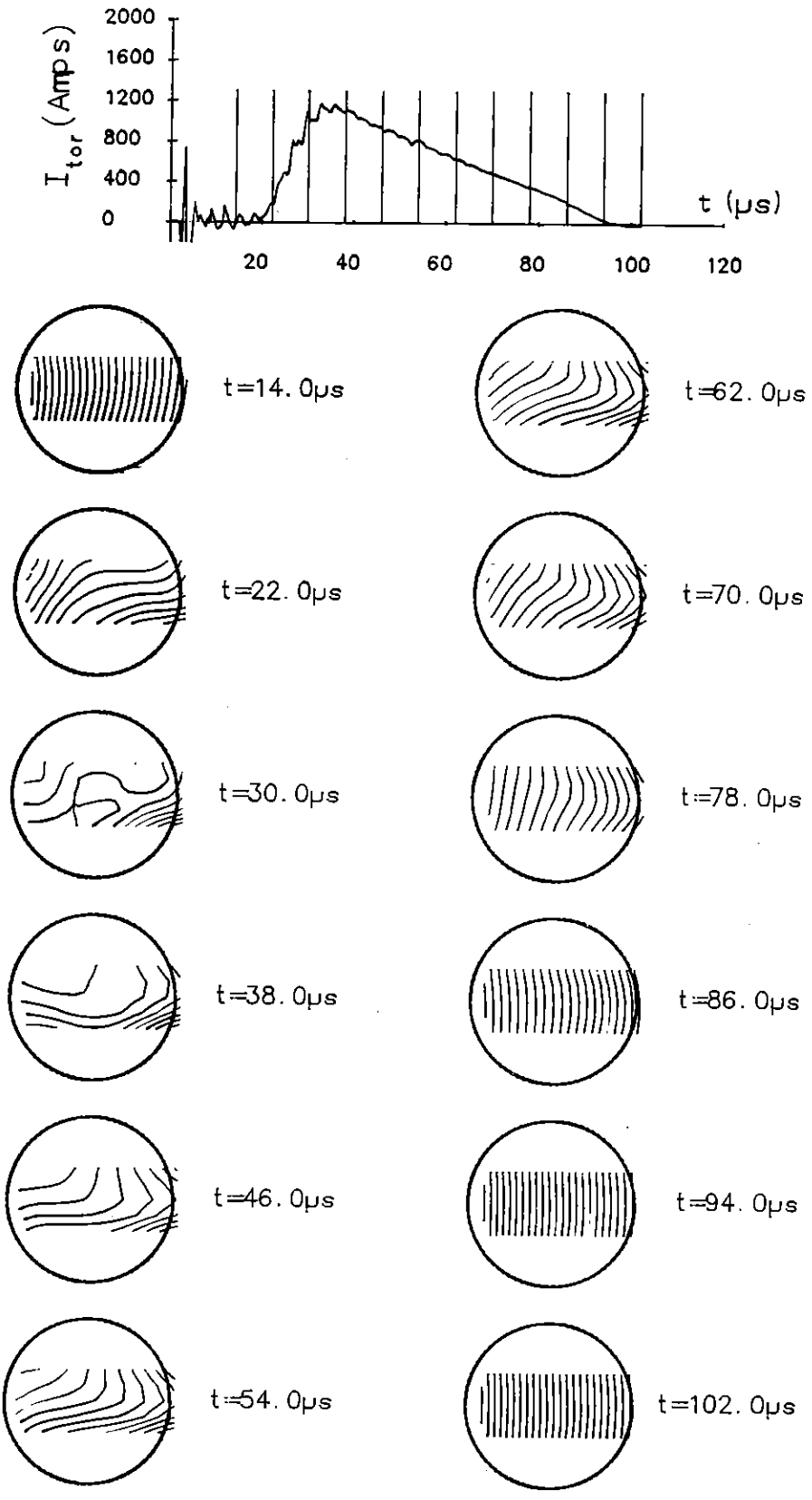

Figure 5.21 Contours of constant poloidal magnetic flux calculated from the polynomial fitted magnetic probe data at equally spaced time intervals during the discharge for Data Set 1. The experimental conditions and the order of the polynomial fit are given in Table 5.4. The position of the vessel wall is indicated by a solid circle. Contour spacing is $6\pi \times 10^{-6}$ Webers.

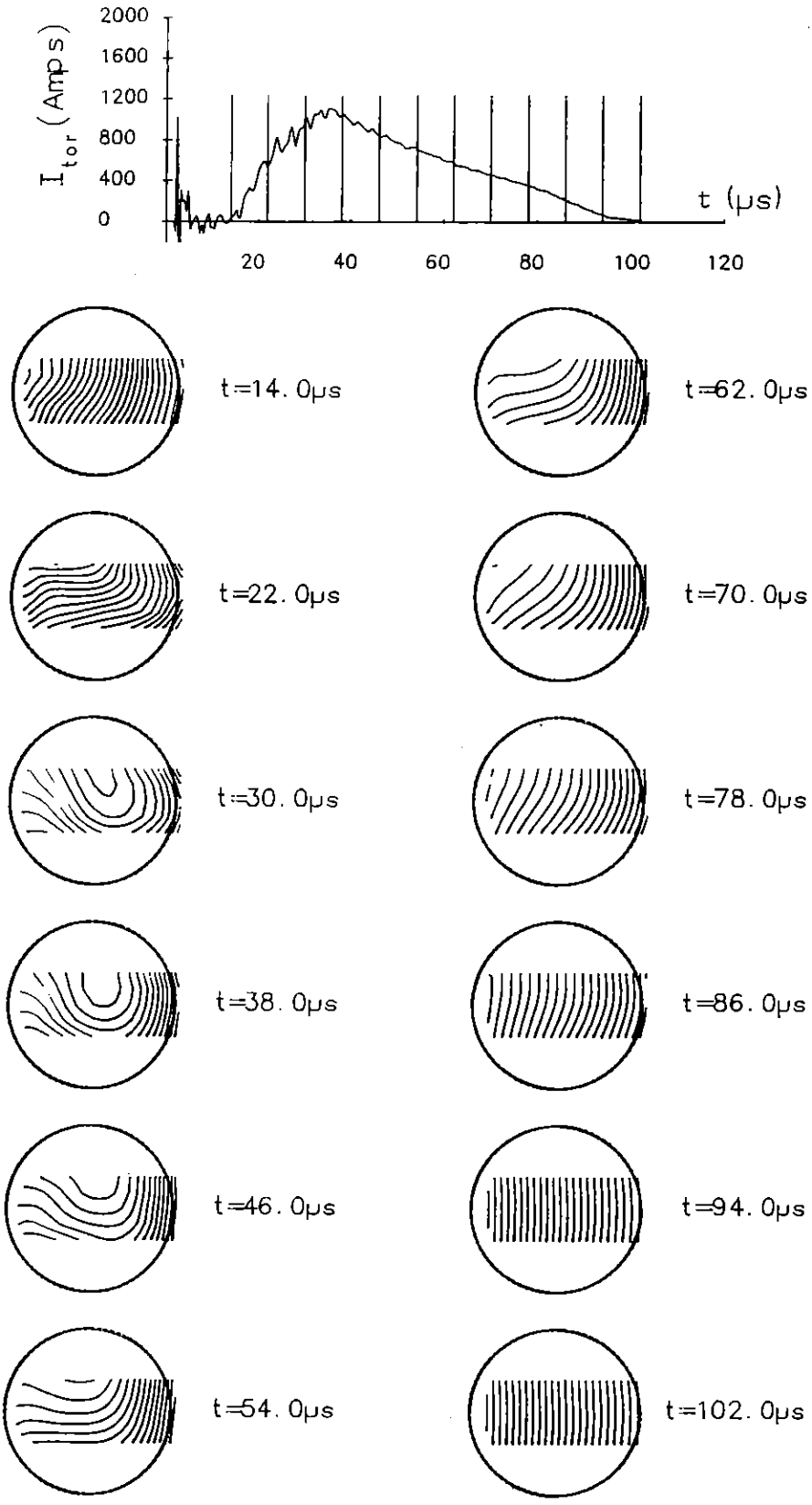

Figure 5.22 Poloidal flux contours for Data Set 2. Toroidal field = 160 G. Contour spacing is $6\pi \times 10^{-6}$ Webers.

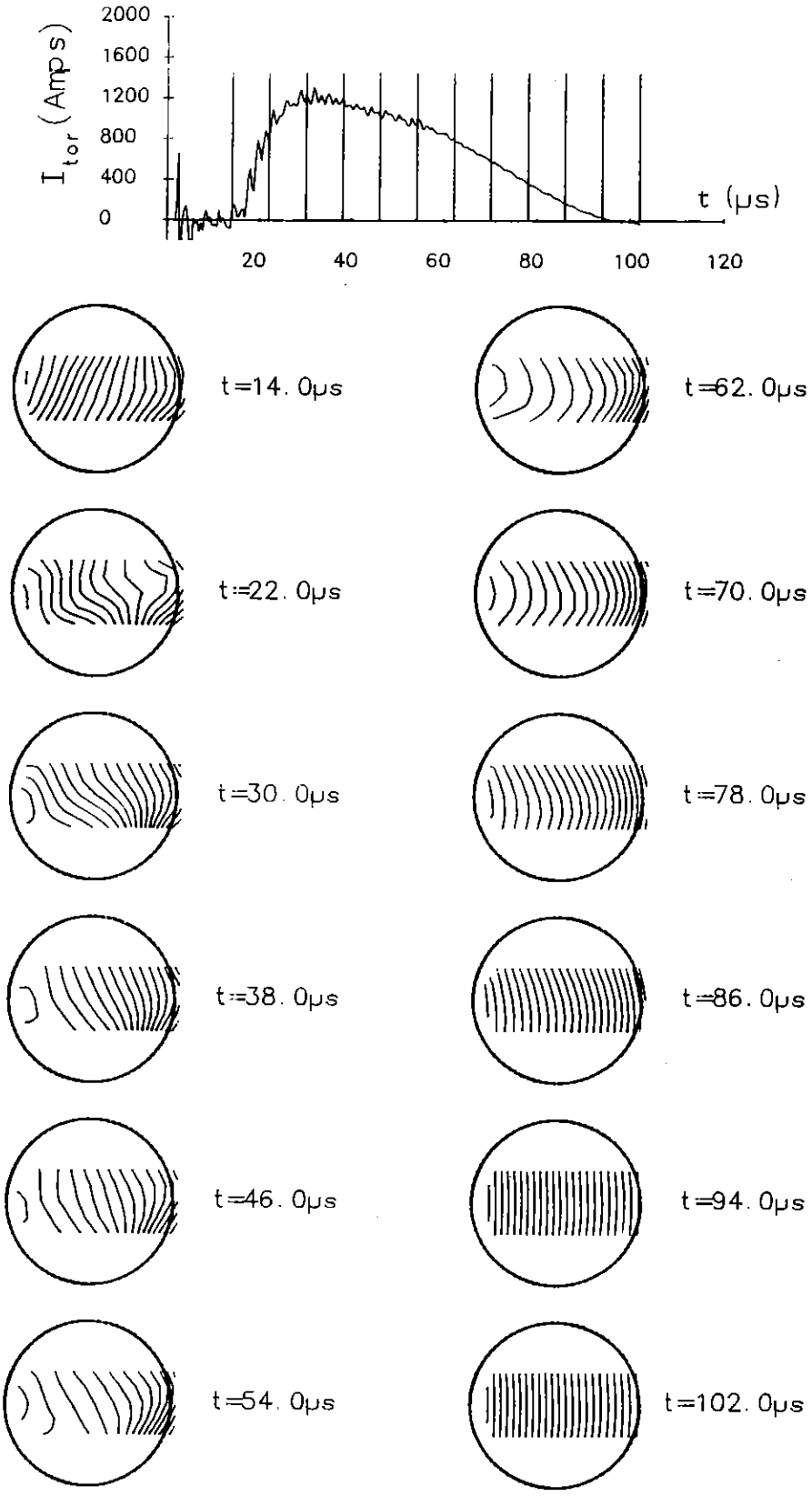

Figure 5.23 Poloidal flux contours for Data Set 3. Toroidal field = −160 G. Contour spacing is $6\pi \times 10^{-6}$ Webers.

toroidal field on the magnetic field structure of double helix current drive discharges in Rythmac-1. The first data set (Data Set 1) was recorded in the absence of an external toroidal magnetic field. Data Sets 2 and 3 were both recorded with a steady toroidal magnetic field of 160G (at $(R_0, 0)$). A positive value of toroidal field is used to indicate a diamagnetic configuration (Data Set 2) in which the toroidal magnetic field produced by the driven poloidal current, ΔB_{tor}, is in the opposite direction to the applied field. A negative value of the external field (Data Set 3) indicates that the direction of the applied field has been reversed, resulting in a paramagnetic configuration.

5.7.3.2 Effect of the RF Phase Velocity.

A pair of experiments was performed to demonstrate that the relative phasing of the RF currents in the external coil structure can be used to control the direction of the driven toroidal (and poloidal) plasma current.

The poloidal flux contours which were obtained for the first of these experiments (Data Set 4: normal diamagnetic configuration) are shown in Figure 5.24. In the second experiment (Data Set 5), the two line generator loads were interchanged in order to reverse the phase velocity on the external structure. To retain a diamagnetic equilibrium configuration, the directions of the external toroidal and vertical magnetic fields were also reversed. The poloidal flux contours obtained for Data Set 5 are presented in Figure 5.25.

The Rogowski belt output signals clearly show that the toroidal current is driven in opposite directions for the two cases. As expected, the polarity of the wirewound probe signals and the calculated poloidal flux was also found to be reversed.

It should be noted that the observed vertical asymmetry in the flux contour plots for the 'normal' and 'reversed' configurations has also changed sign. This observation seems to indicate that the asymmetry is not caused by a slight misalignment of the

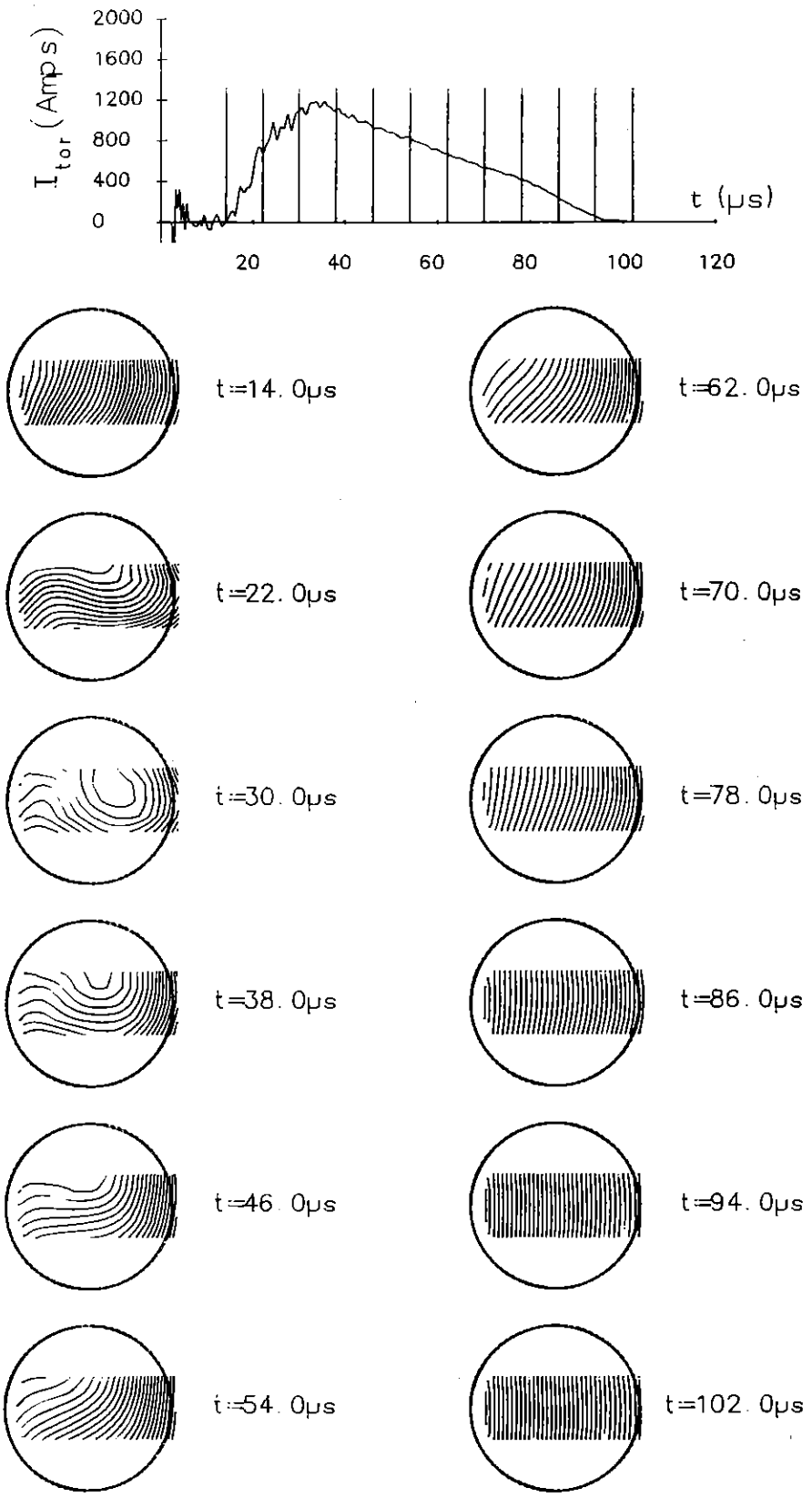

Figure 5.24 Poloidal flux contours for Data Set 4: 'Normal' configuration. Contour spacing is $6\pi \times 10^{-6}$ Webers.

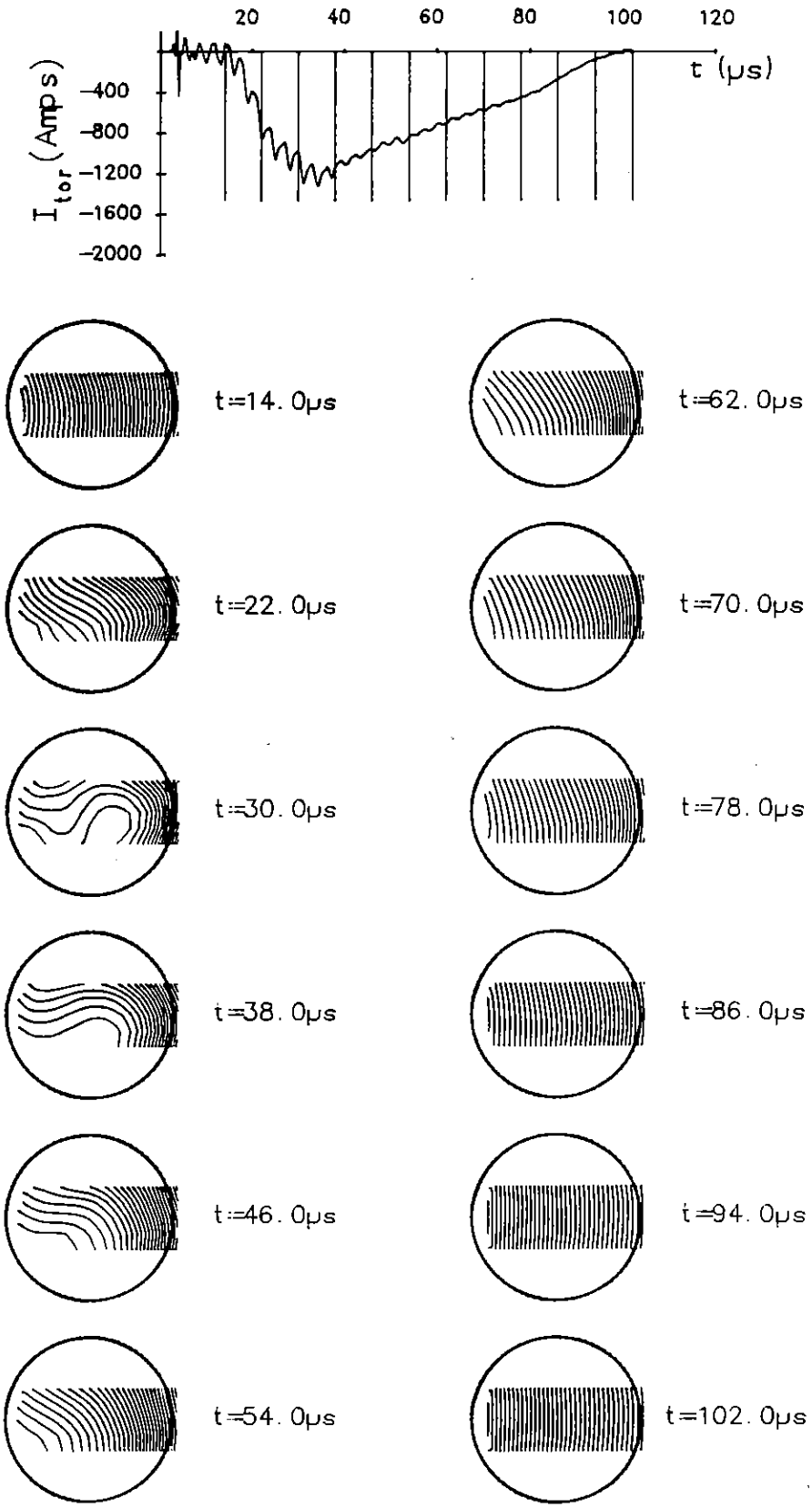

Figure 5.25 Poloidal flux contours for Data Set 5: 'Reversed' configuration.

Contour spacing is $6\pi \times 10^{-6}$ Webers.

vacuum vessel or external field coils.

5.7.3.3 Comparison of Ψ and ΔB_{tor} Contour Plots.

In Figure 5.26a and Figure 5.26b, we show contour plots of the poloidal flux function (Ψ) and quasi-steady toroidal magnetic field (ΔB_{tor}) which have been constructed from detailed magnetic probe data collected under the same experimental conditions in Rythmac-1. These plots are presented as Data Set 6 in Table 5.4.

The toroidal magnetic field contour plots shown in Figure 5.26b are constructed from the raw probe data. A two-dimensional polynomial fit to the raw ΔB_{tor} data with r and z polynomial fitting orders of $N_1 = 6$, $N_2 = 6$, yields the contour plots shown in Figure 5.26c.

In Figure 5.26b and Figure 5.26c, we display the time dependence of both the driven toroidal current and the change in the toroidal magnetic field associated with the driven poloidal current. The change in the toroidal magnetic field was measured at the centre of the minor section ($r = R_0, z = 0$) with the wirewound probe. The apparent time delay of approximately $6\mu s$ between the peak toroidal and peak poloidal current is not real. The delay is introduced by the lowpass filter described in Section 4.2, which is used to condition the raw magnetic probe signal.

The time behaviour of the quasi-steady toroidal and poloidal current is seen to be different; the poloidal current is not maintained for the entire duration of the RF pulse. From Figure 5.2, it is evident that the driven toroidal and poloidal plasma currents reach their maximum values at the time of peak external RF current (i.e. peak available RF power). After this time, the driven poloidal current decreases much more rapidly with time than the toroidal current. This behaviour is believed to be a consequence of the decline in available RF power during the shot (also evident from Figure 5.2). Since the poloidal plasma current is driven over a larger cross sectional area than the toroidal plasma current (and I_{pol} is more than an order of magnitude

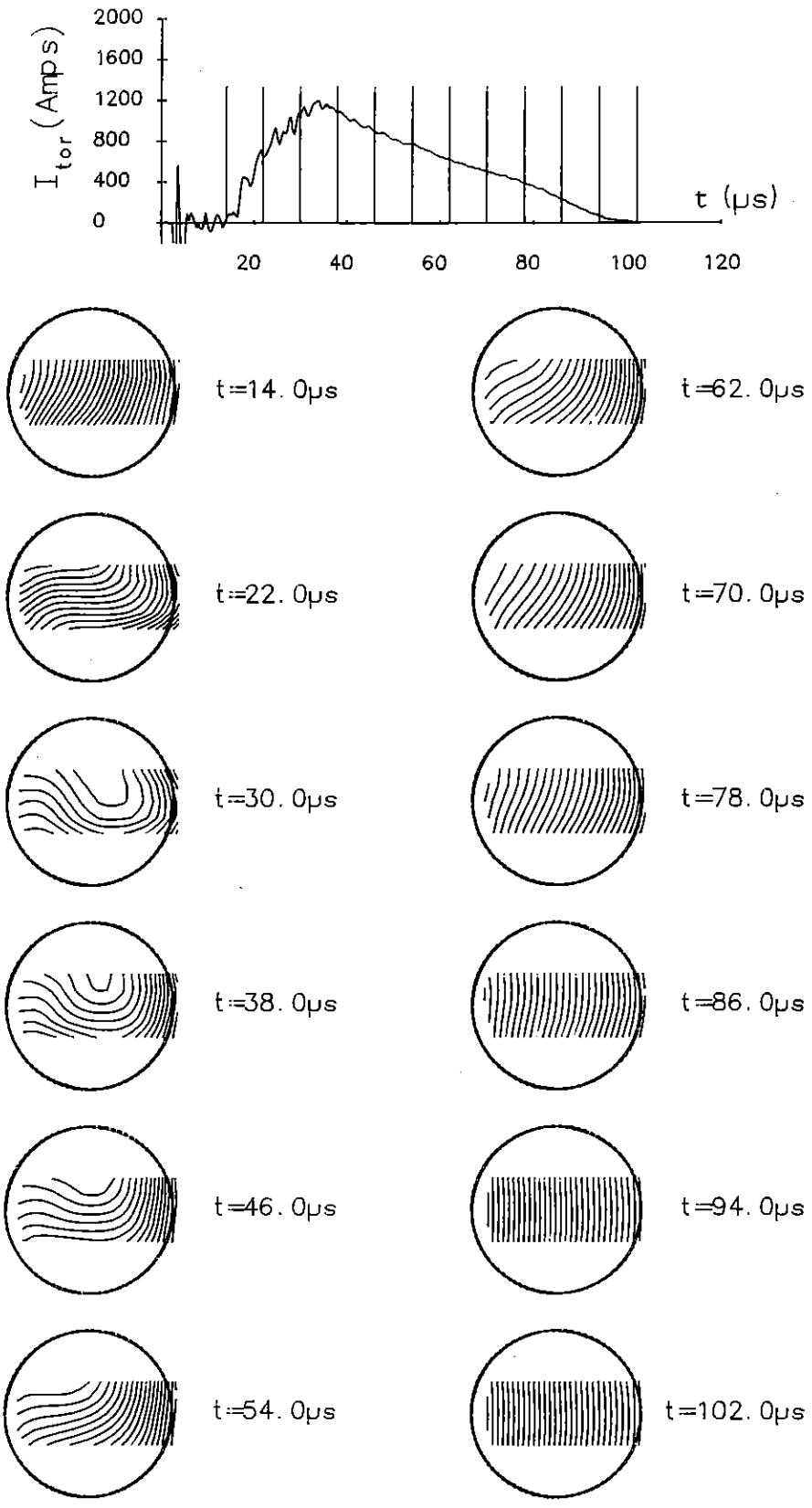

Figure 5.26a Poloidal flux contours for Data Set 6.

Contour spacing is $6\pi \times 10^{-6}$ Webers.

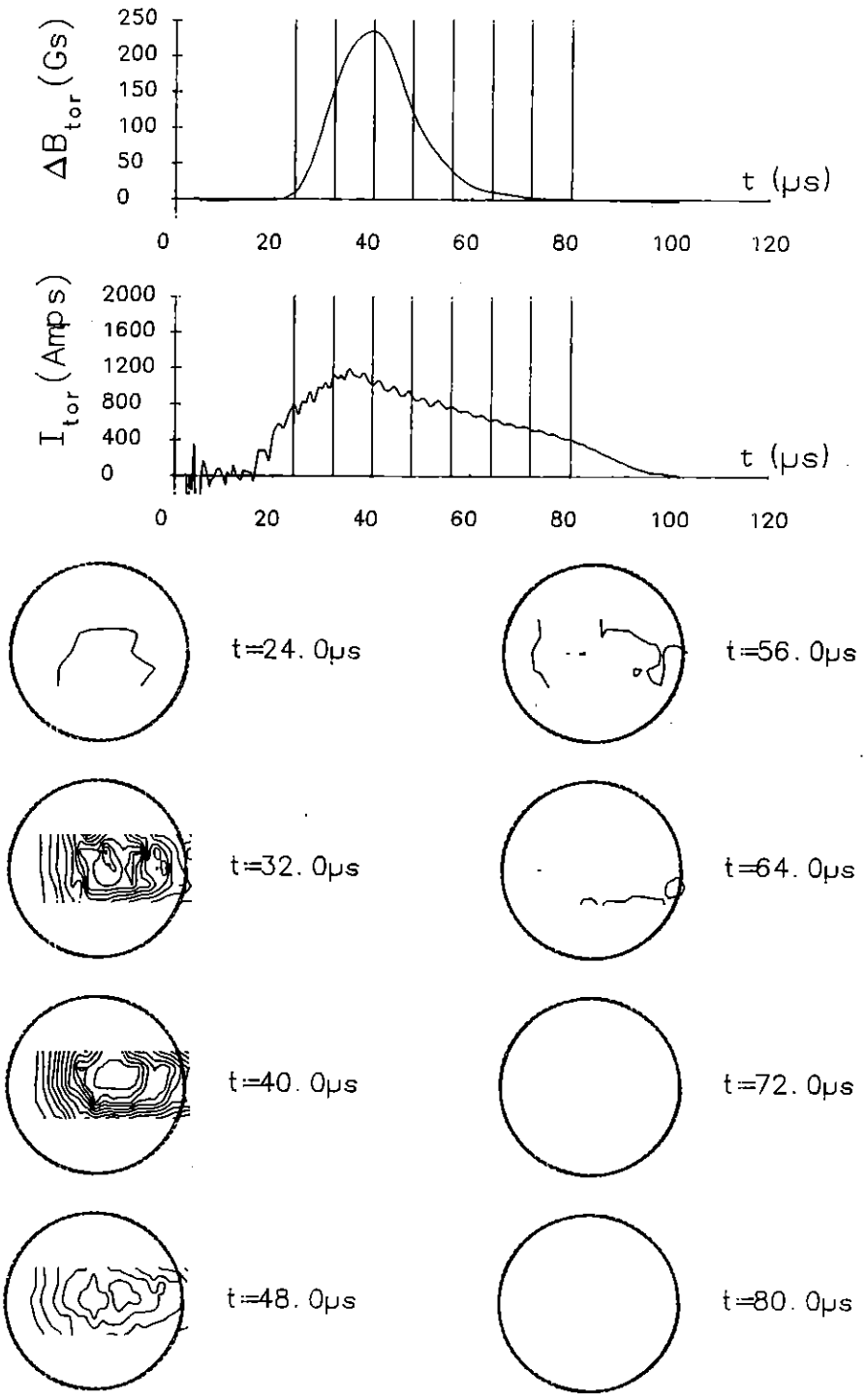

Figure 5.26b Contour plot of the change in the quasi-steady toroidal magnetic field, ΔB_{tor}, produced by the driven poloidal current for Data Set 6. The contour plots are constructed from the raw magnetic field data. The contour spacing is 20 Gauss.

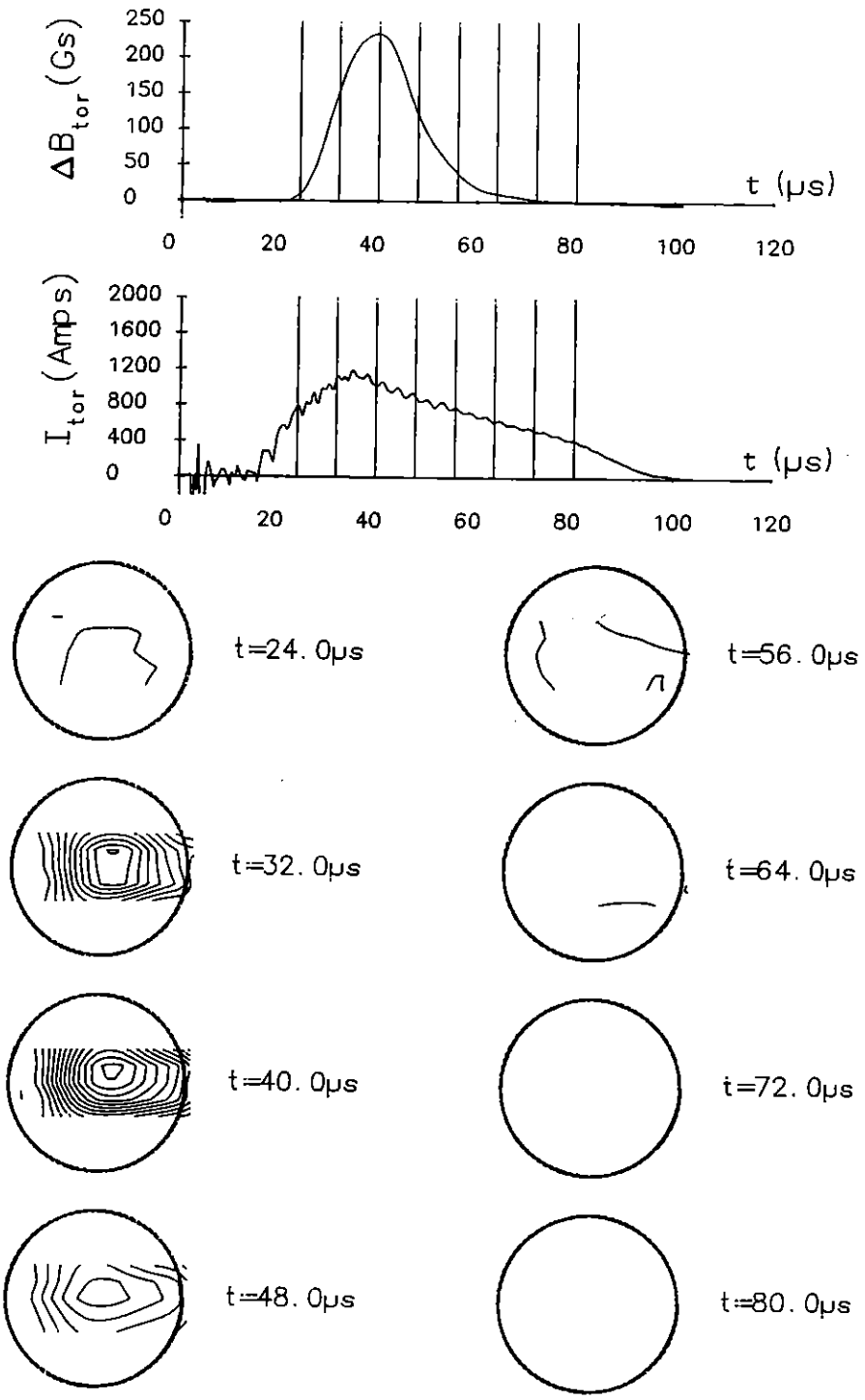

Figure 5.26c Contour plot of the change in the quasi-steady toroidal magnetic field, ΔB_{tor}, produced by the driven poloidal current for Data Set 6. The contour plots are constructed from the polynomial fitted magnetic probe data, with $N_1 = 6, N_2 = 6$. The contour spacing is 20 Gauss.

larger than I_{tor}), the poloidal plasma current is expected to be more sensitive to reductions in the level of available RF power.

5.7.3.4 The Helical Mesh Antenna.

Flux contours obtained using the helical mesh antenna in Rythmac-2 (Data Sets 7,8) are plotted in Figure 5.27a and Figure 5.28.

Although the helical mesh antenna was designed to drive purely toroidal current, some residual poloidal current was observed in the experiments. In Figure 5.27a (Data Set 7), the external toroidal magnetic field was found to produce a slightly paramagnetic configuration, whilst in Figure 5.28 (Data Set 8), the direction of the applied toroidal field was reversed so that a slightly diamagnetic configuration was produced. Contour plots of ΔB_{tor} which were measured for the slightly paramagnetic configuration are presented in Figure 5.27b. The raw ΔB_{tor} measurements have been fitted as in the previous section using a two-dimensional polynomial in (r, z) with $N_1 = 6, N_2 = 6$.

A comparision of Figure 5.26c and Figure 5.27b clearly indicates that a much smaller ΔB_{tor} is produced by the helical mesh antenna compared to the $m = 1$ double helix antenna. The value of ΔB_{tor} produced by the helical mesh antenna at the centre of the minor section is smaller by a factor of about 8, despite the fact that the helical mesh drives $\sim 30\%$ more toroidal current than the double helix antenna under the same conditions.

5.7.3.5 Flux Contours at Two Different Toroidal Locations.

Detailed magnetic probe measurements were made under the same discharge conditions at two different toroidal locations (separated by 90^0) in the Rythmac-3 device.

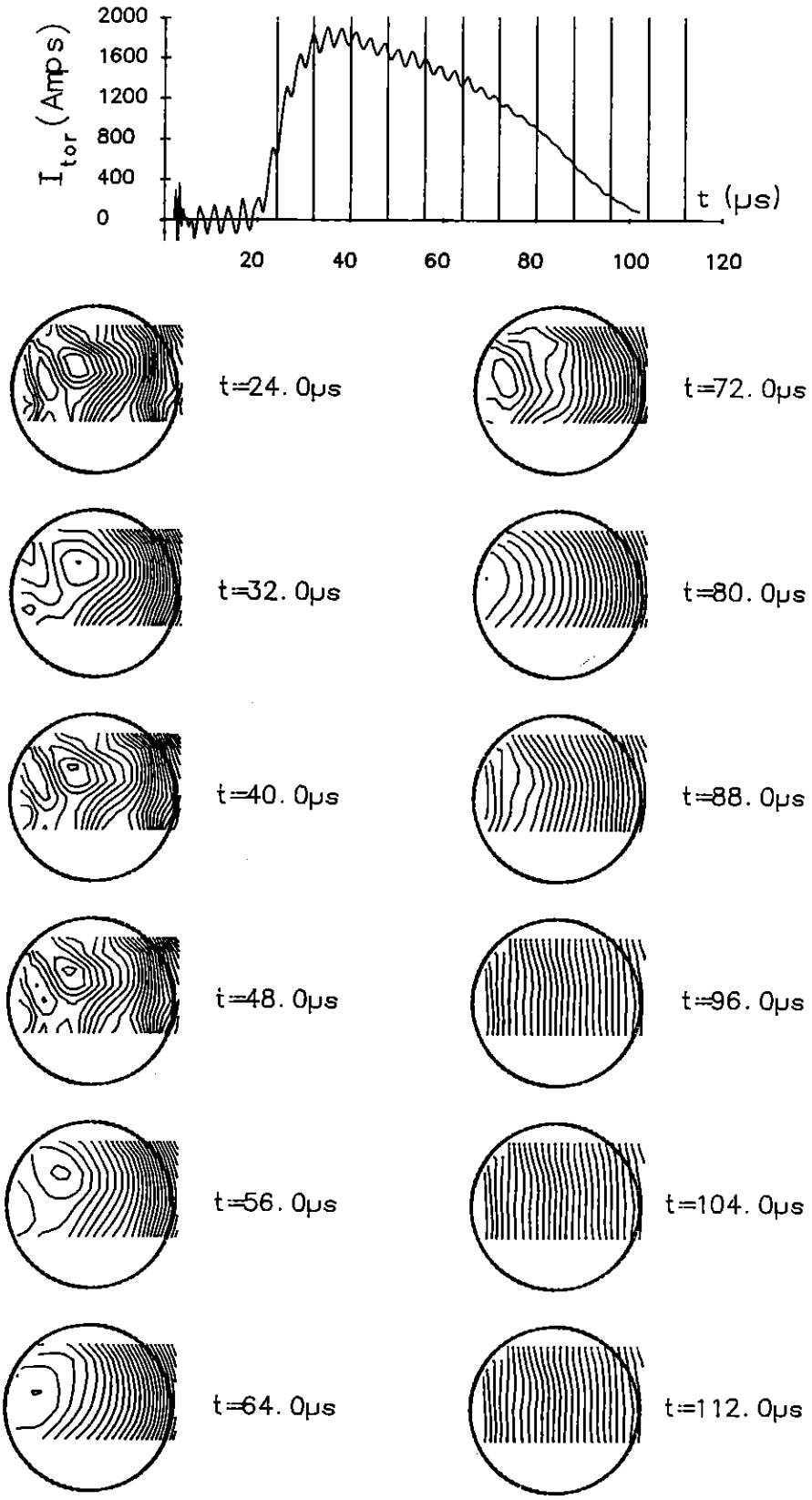

Figure 5.27a Poloidal flux contours obtained with the helical mesh antenna. Data Set 7 (slightly paramagnetic configuration). The contour spacing is $10\pi \times 10^{-6}$ Webers.

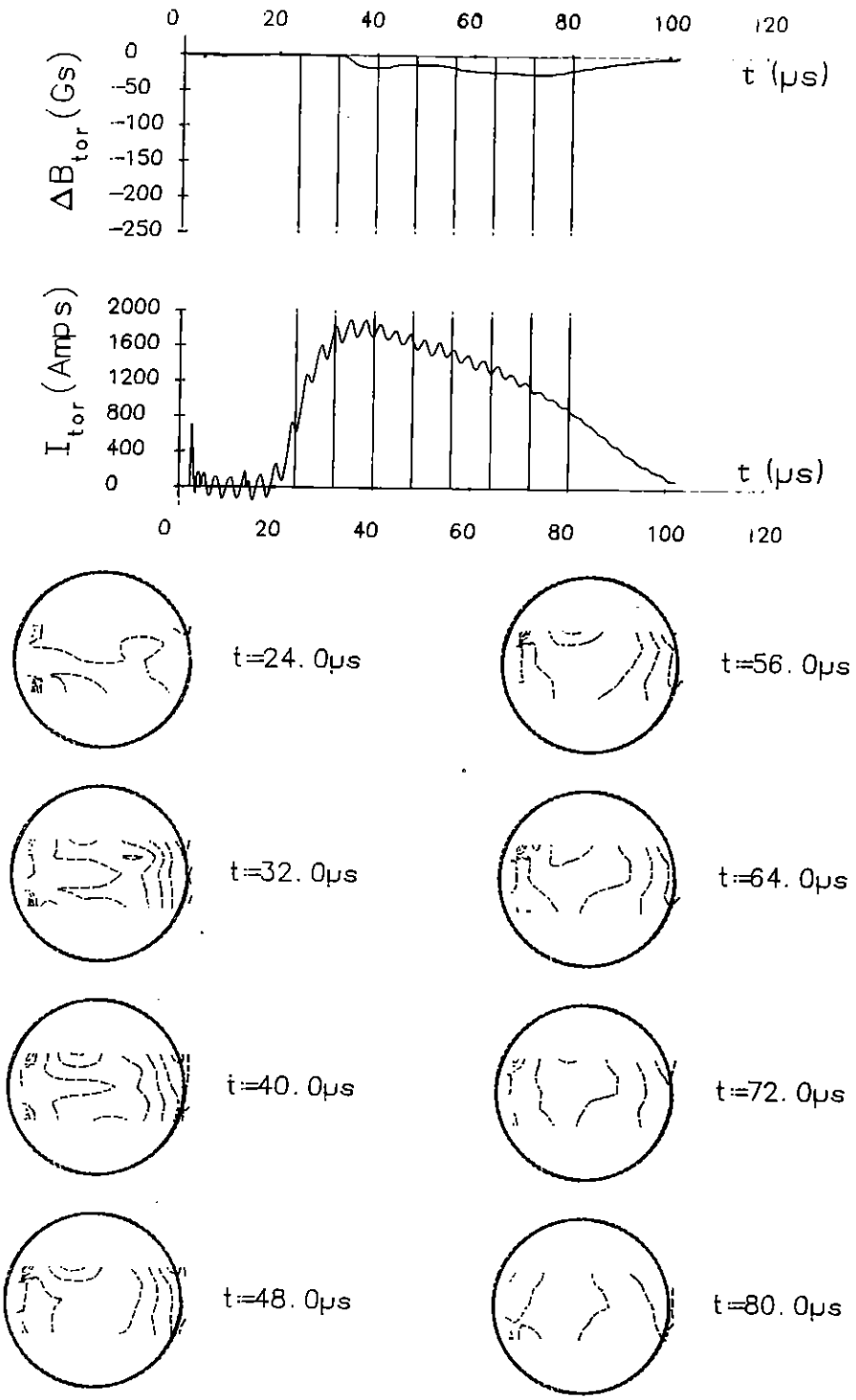

Figure 5.27b Contour plot of the change in the quasi-steady toroidal magnetic field, ΔB_{tor}, for Data Set 7, using the helical mesh antenna. The contour plots are constructed from the polynomial fitted magnetic probe data, with $N_1 = 6, N_2 = 6$. The contour spacing is 20 Gauss.

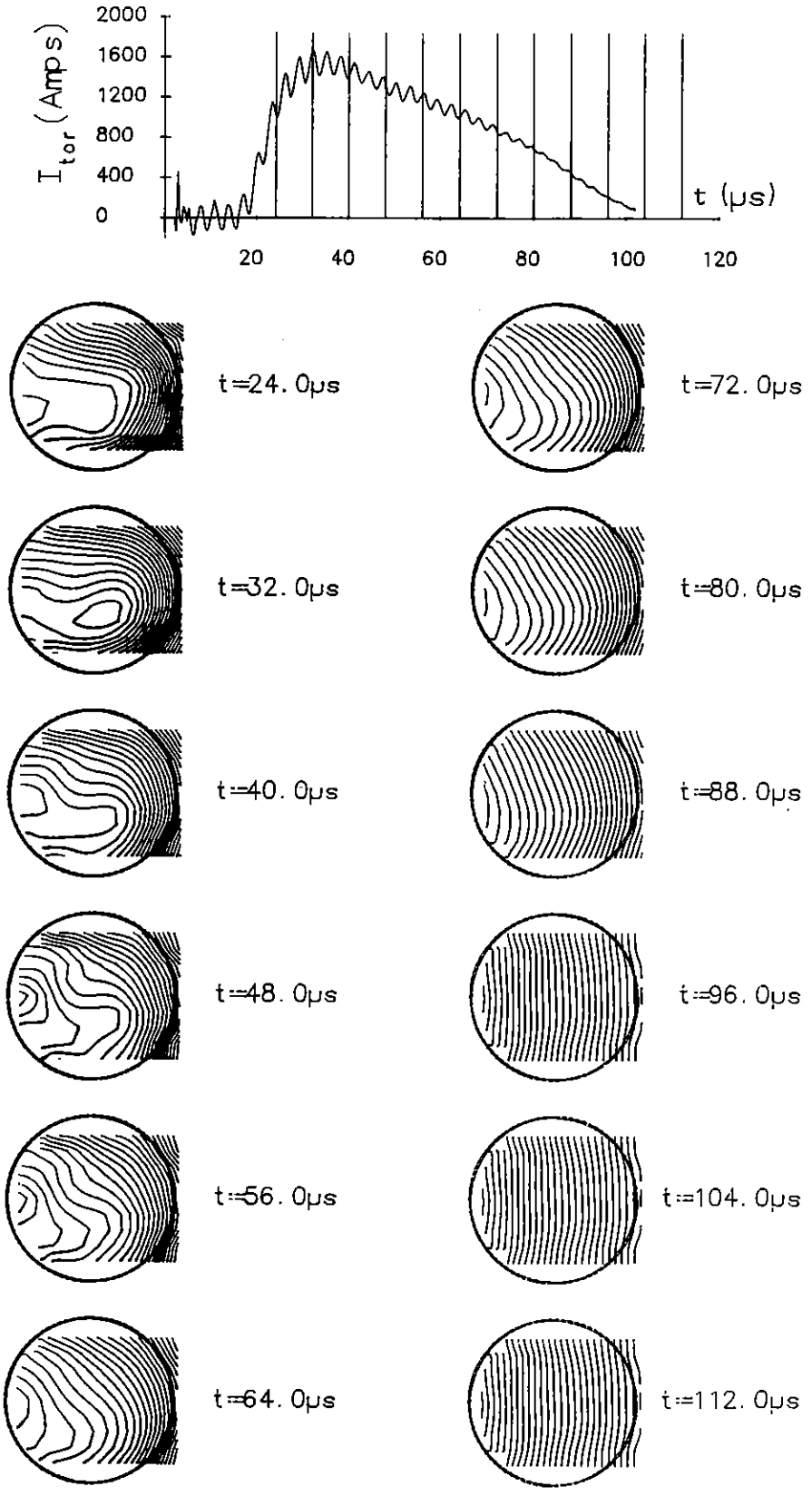

Figure 5.28 Poloidal flux contours for the slightly diamagnetic configuration produced with the helical mesh antenna (Data Set 8). The contour spacing is $10\pi \times 10^{-6}$ Webers.

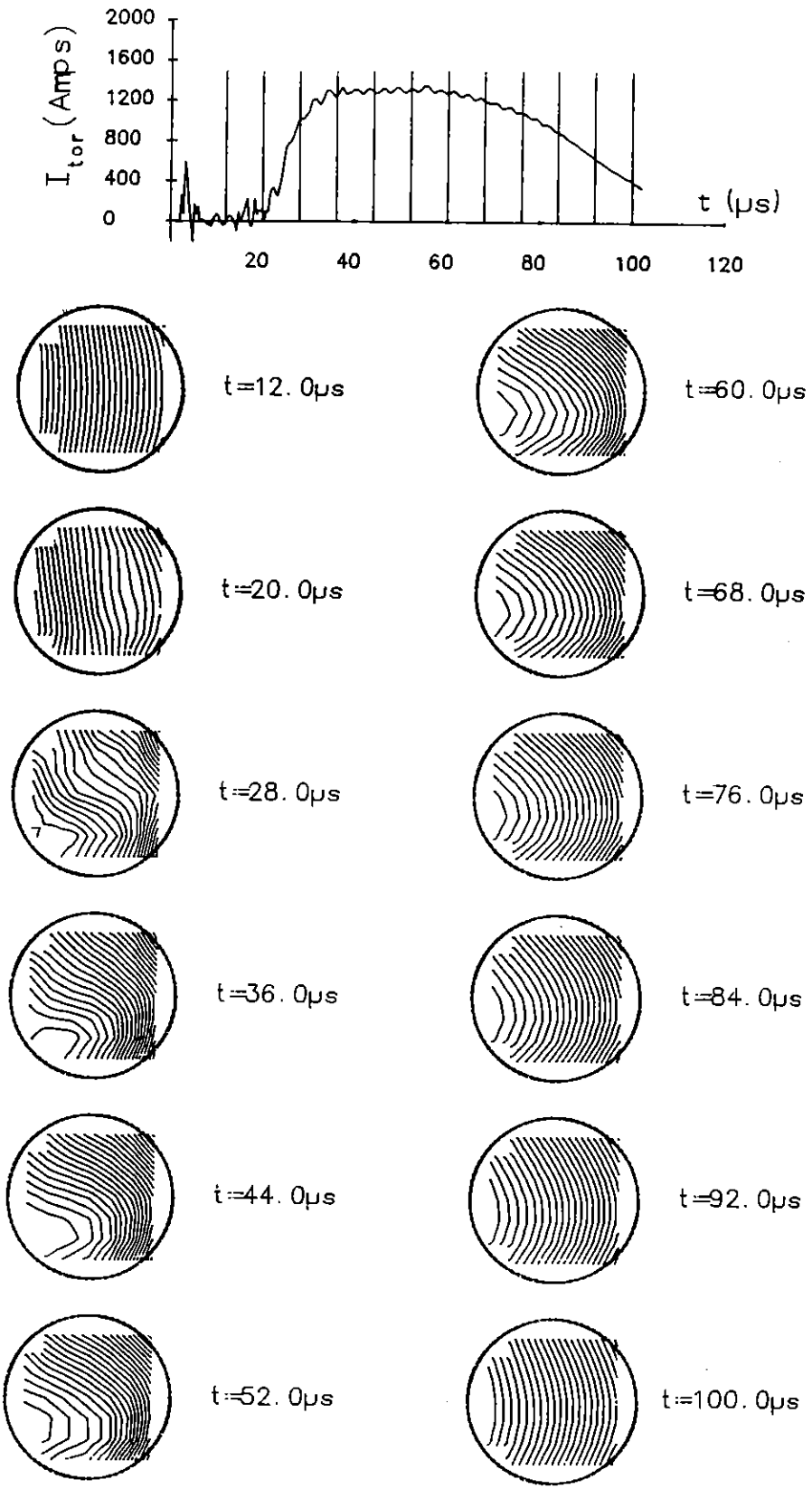

Figure 5.29 Poloidal flux contours for Data Set 9. MACOR block 1.

Contour spacing is $16\pi \times 10^{-6}$ Webers.

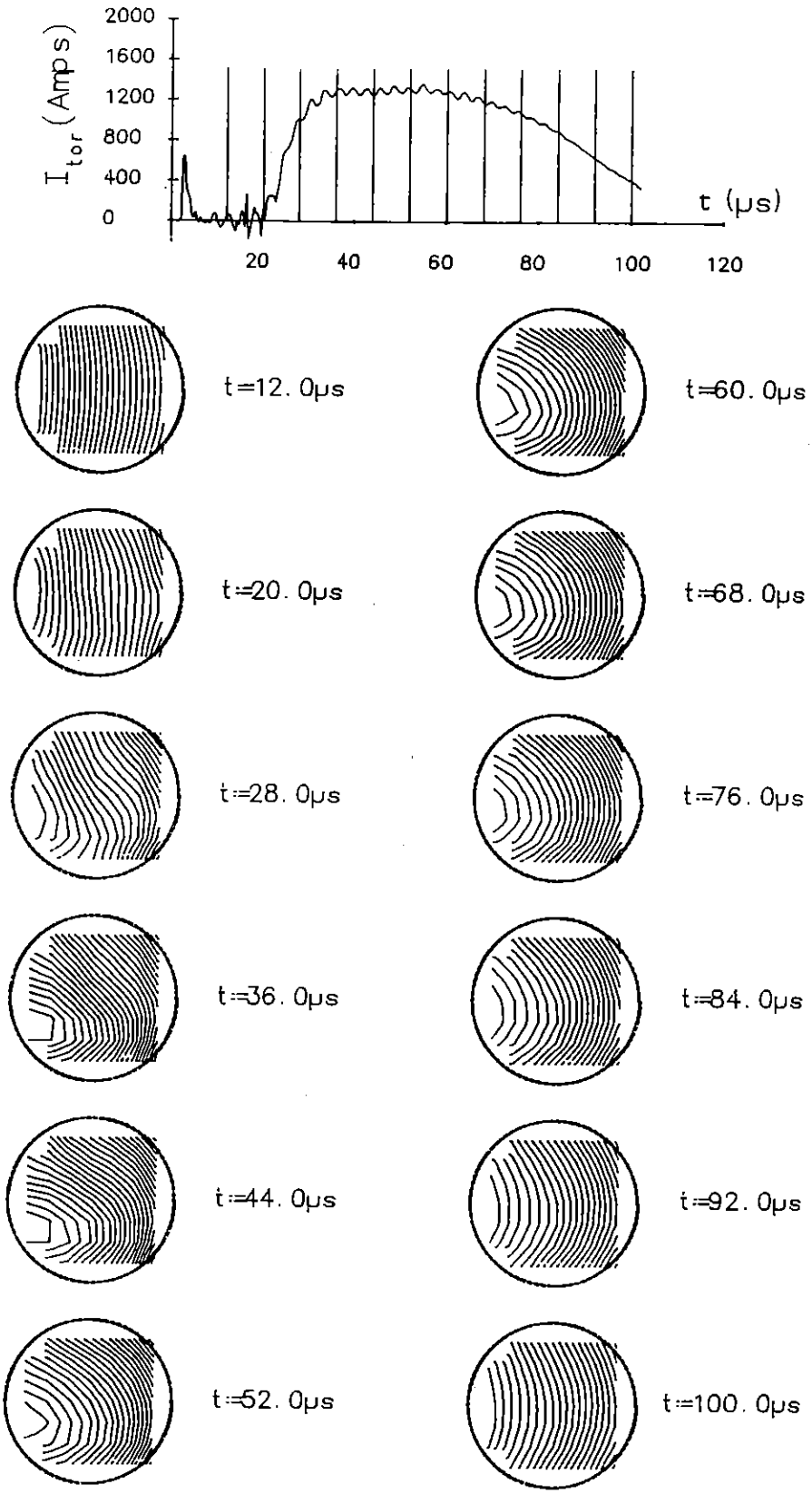

Figure 5.30 Poloidal flux contours for Data Set 10. MACOR block 2. Contour spacing is $16\pi \times 10^{-6}$ Webers.

The measurements were made using two arrays of horizontal probe guides, which could be inserted into the minor section of the vessel through the MACOR block assemblies provided. The poloidal flux contours for these two locations (Data Sets 9 and 10) are shown in Figure 5.29 and Figure 5.30.

The two sets of contour plots are clearly very similar. As previously mentioned, the locations at which the poloidal flux contours were measured were separated by 90^0 in the toroidal direction, whereas the toroidal mode number of the external coils was $n = 6$. Hence, the orientation of the RF coils is different at the two locations. The fact that the same asymmetry was observed in the poloidal flux contours measured at the two locations suggests that the asymmetry is global rather than helical.

5.7.3.6 Effect of the Steady Vertical Magnetic Field.

In hindsight, it appears that in the majority of the preceding poloidal flux contour Data Sets the applied vertical field was excessively large. As a result, very few closed poloidal flux contours were observed in these experiments.

The minimum value of the vertical magnetic field was determined by the smallest voltage at which the slow capacitor bank would operate reliably. The minimum vertical magnetic field which could be obtained in this manner was $B_v \simeq 30$G. Larger values of the vertical field were used in an attempt to force the driven toroidal plasma current away from the outer wall of the vessel and into the centre of the minor section.

In order to substantially reduce the strength of the applied vertical magnetic field, the slow capacitor bank was subsequently replaced by a DC power supply as described in Section 3.4.

A series of three experiments were conducted to gauge the effect of the vertical magnetic field on the nature of the poloidal flux contour plots. The values of the vertical field used in these experiments were relatively low, differing by approximately 8% about a mean value of 9.3G. All other discharge conditions were the same for each

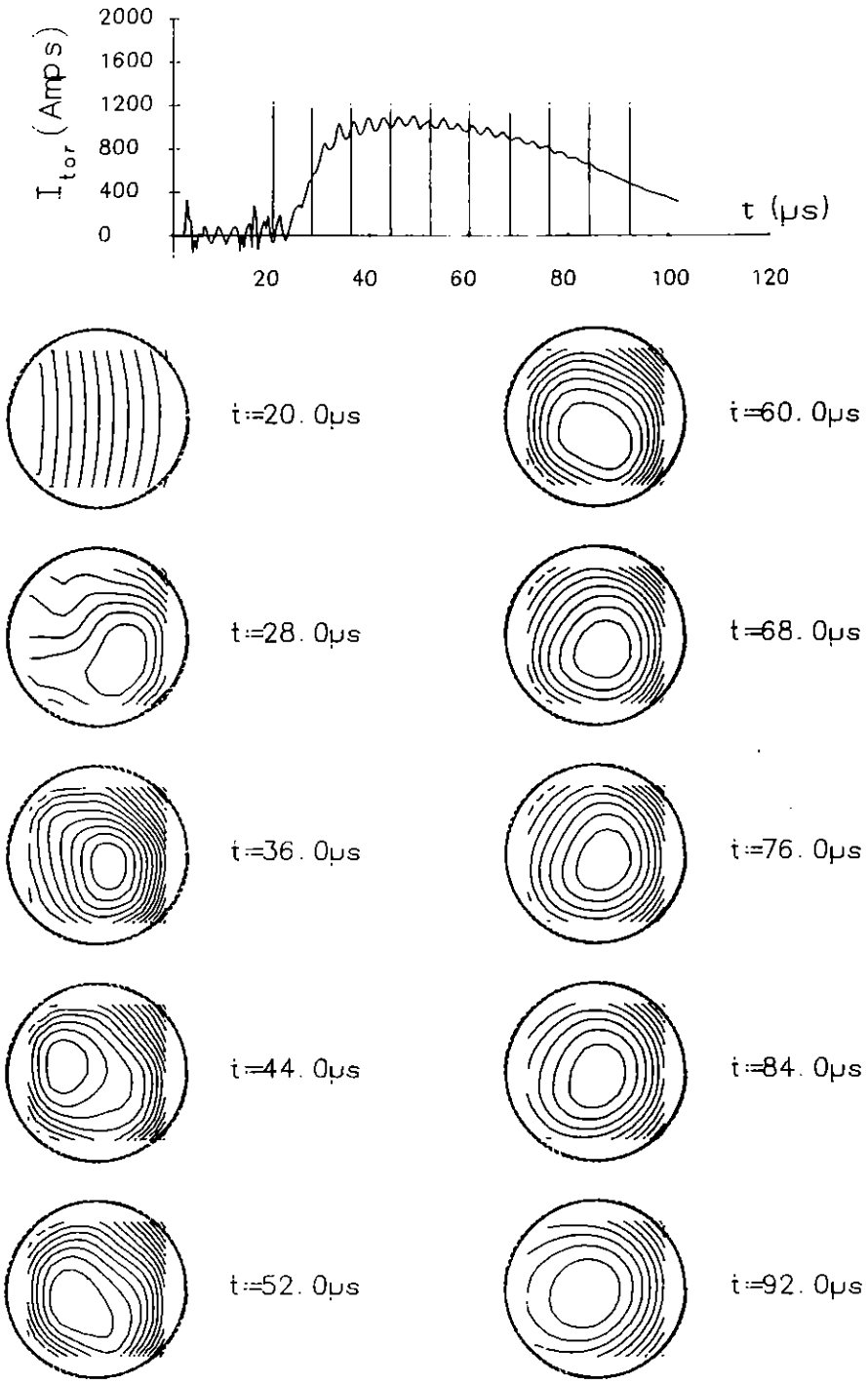

Figure 5.31 Poloidal flux contours for Data Set 11. Vertical field = 8.5G. Contour spacing is $8\pi \times 10^{-6}$ Webers.

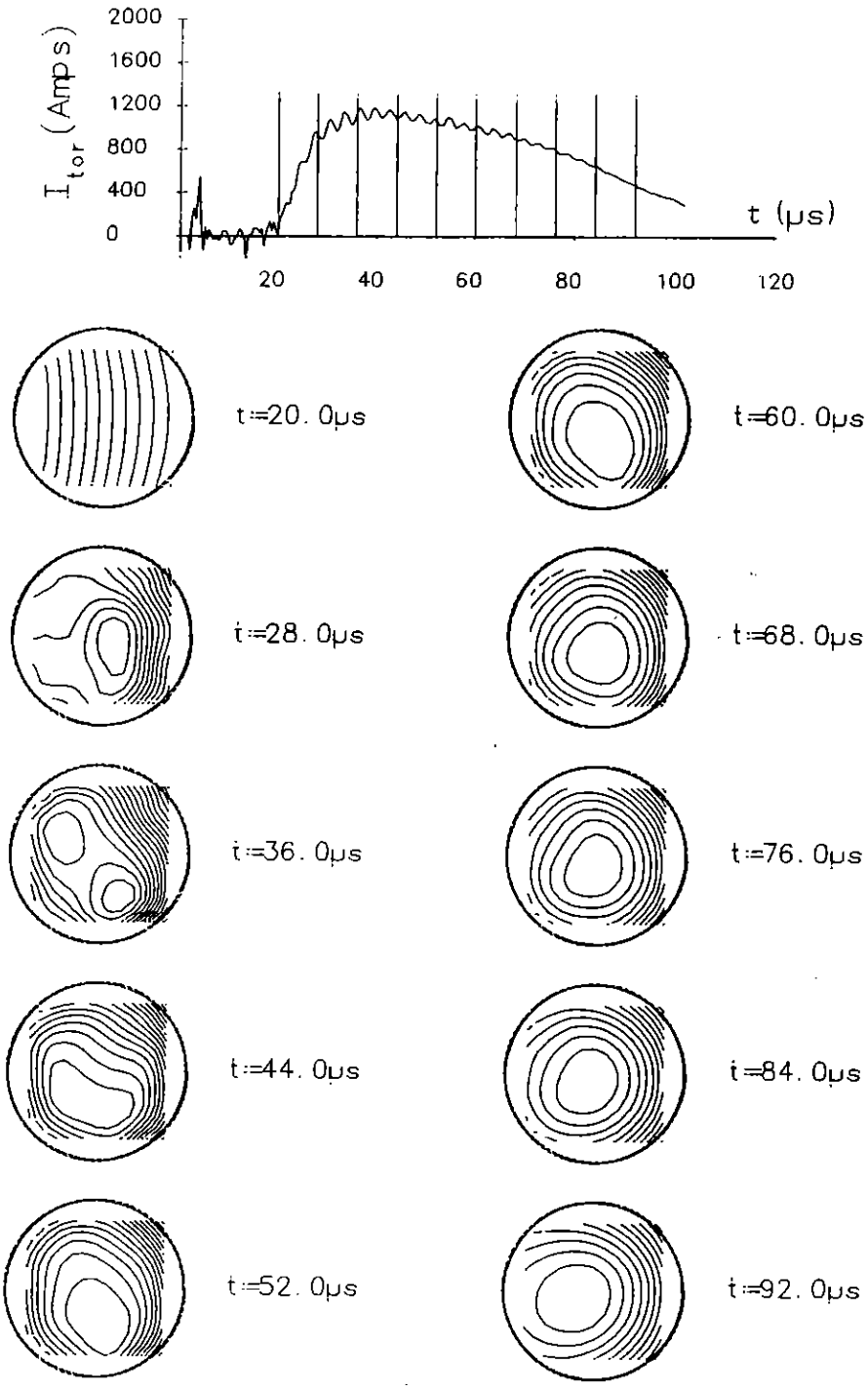

Figure 5.32a Poloidal flux contours for Data Set 12. Vertical field = 9.3G. Contour spacing is $8\pi \times 10^{-6}$ Webers.

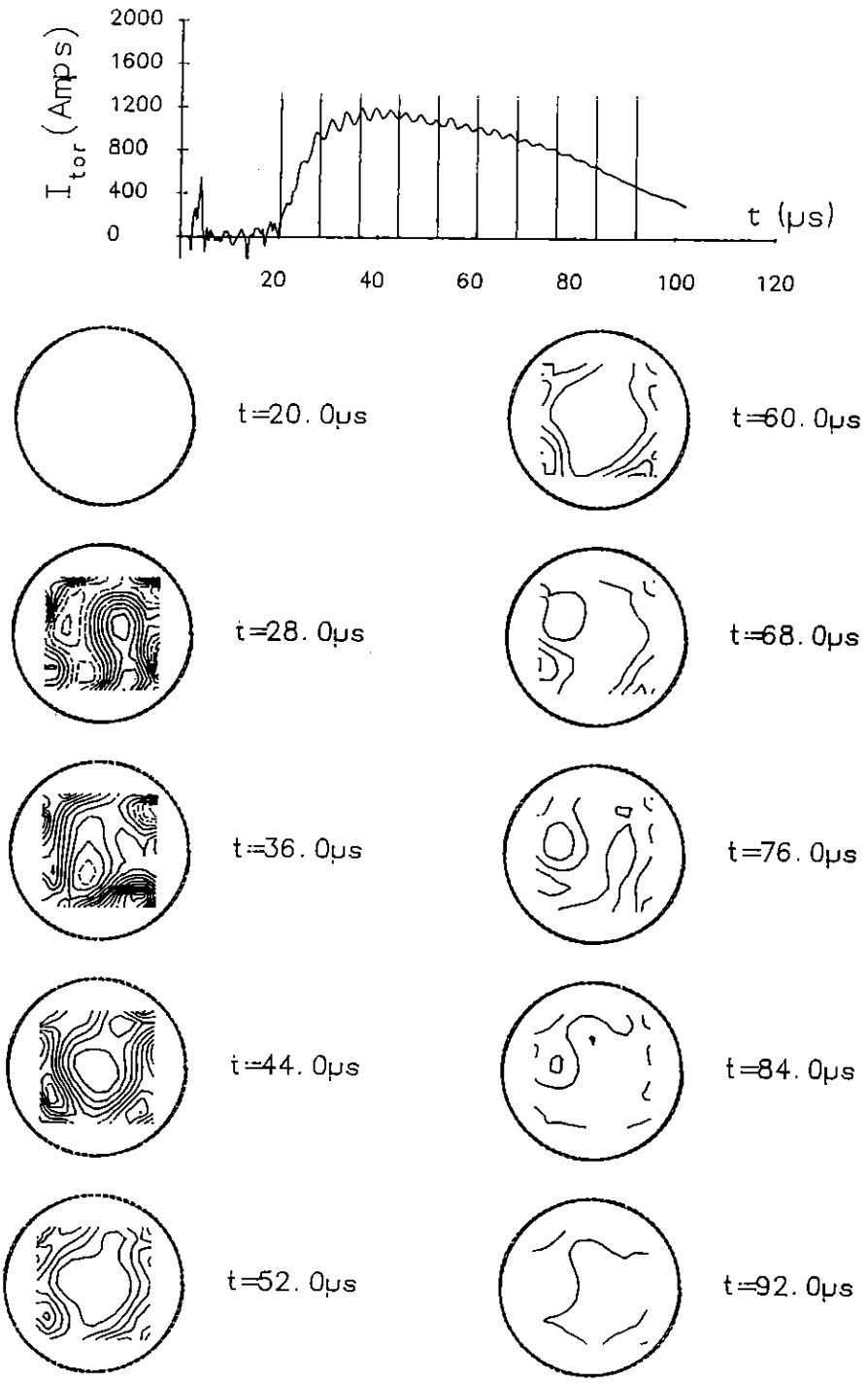

Figure 5.32b Contours of constant toroidal current density for Data Set 12. Broken contours indicate regions of negative current density. The contour spacing is 20000 A/m^2.

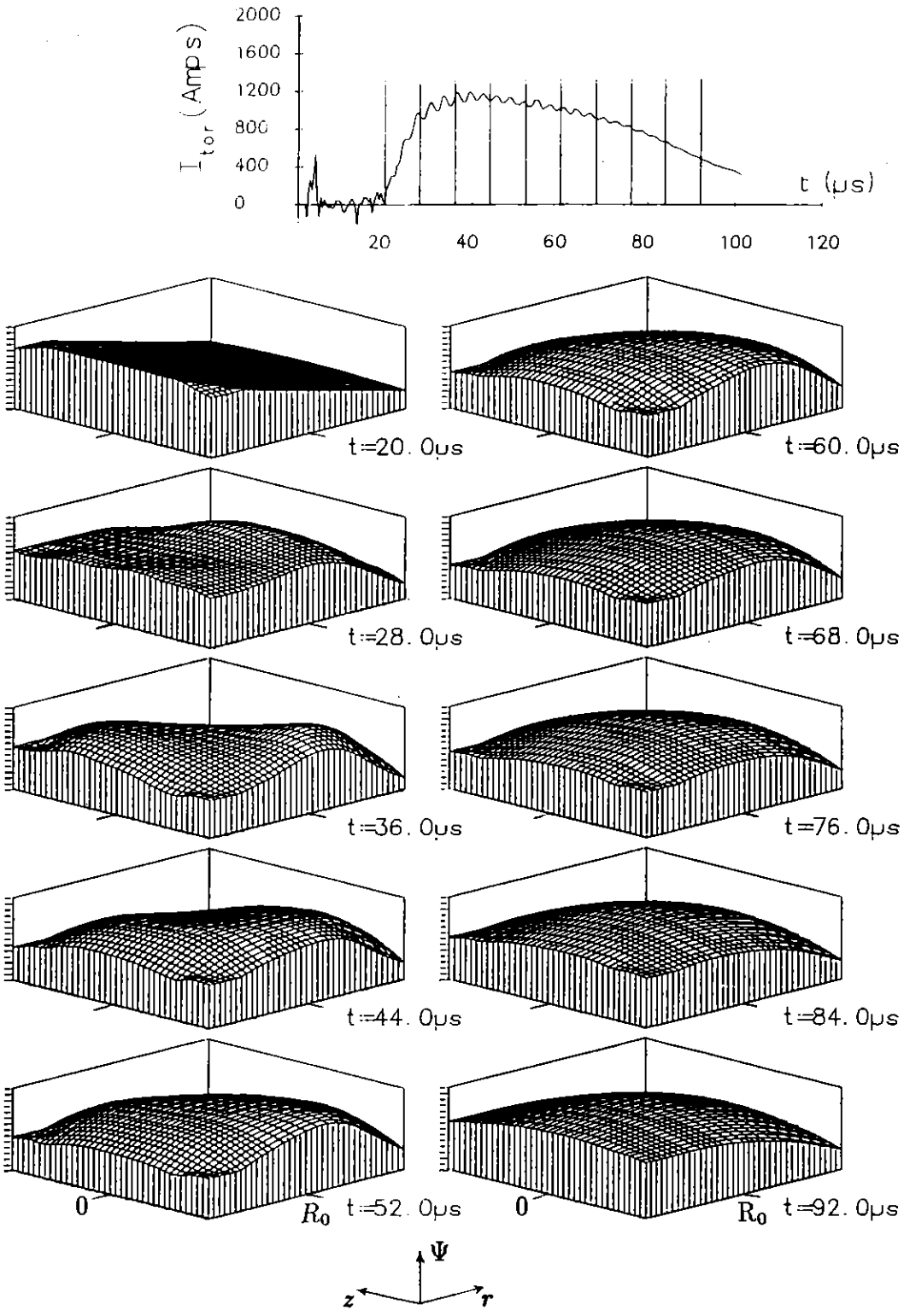

Figure 5.32c Three dimensional surface plots of the poloidal flux function (shown as contour plots in Figure 5.32a) at equal time intervals during the discharge for Data Set 12. The vertical scale is $10\pi \times 10^{-6}$ Webers per division and the grid spacing is 0.33cm. The flux values have been inverted to improve presentation.

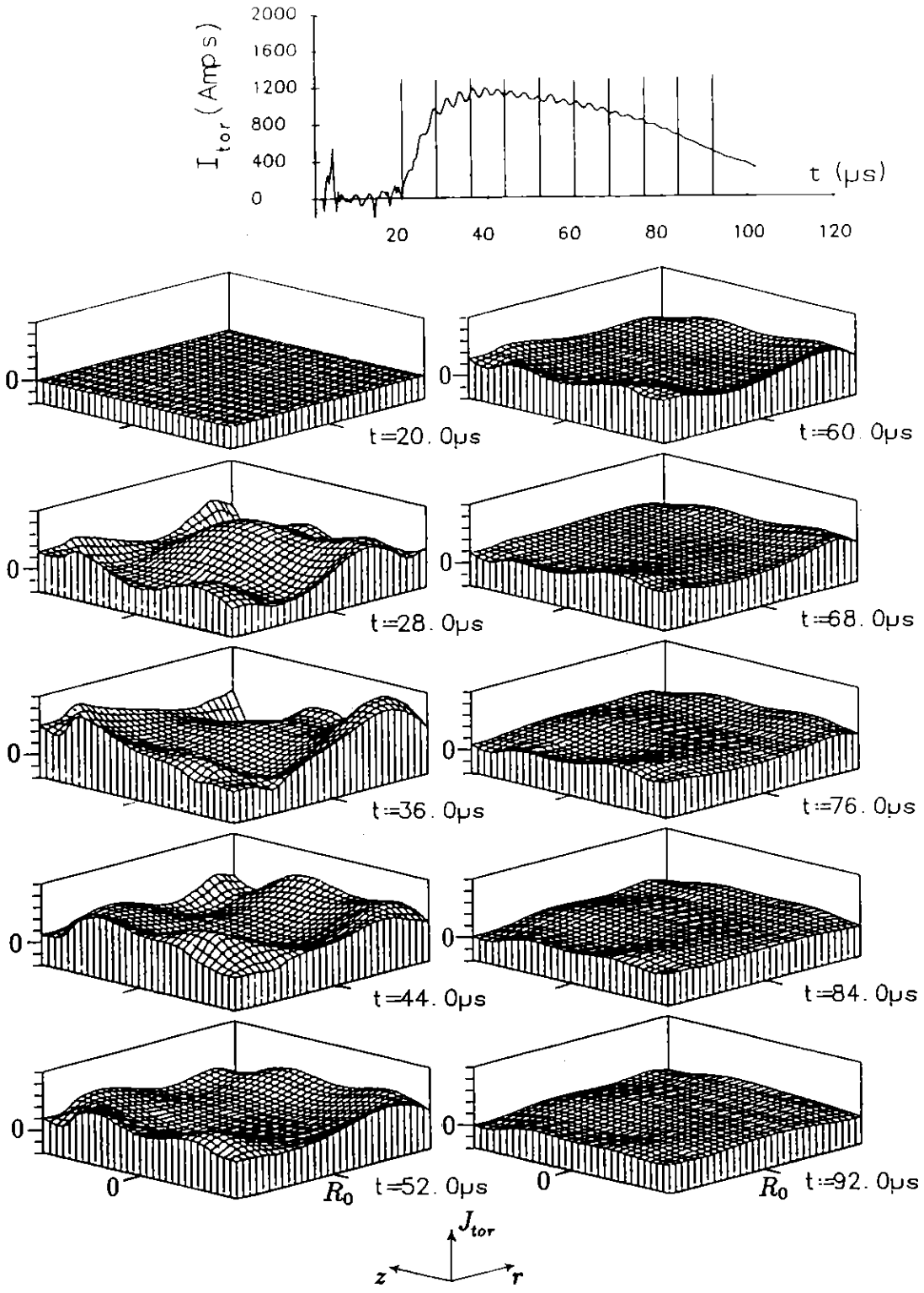

Figure 5.32d Three dimensional surface plots of the toroidal current density (shown as contour plots in Figure 5.32b) for Data Set 12. The vertical scale is 50000 A/m^2 per division and the grid spacing is 0.33cm.

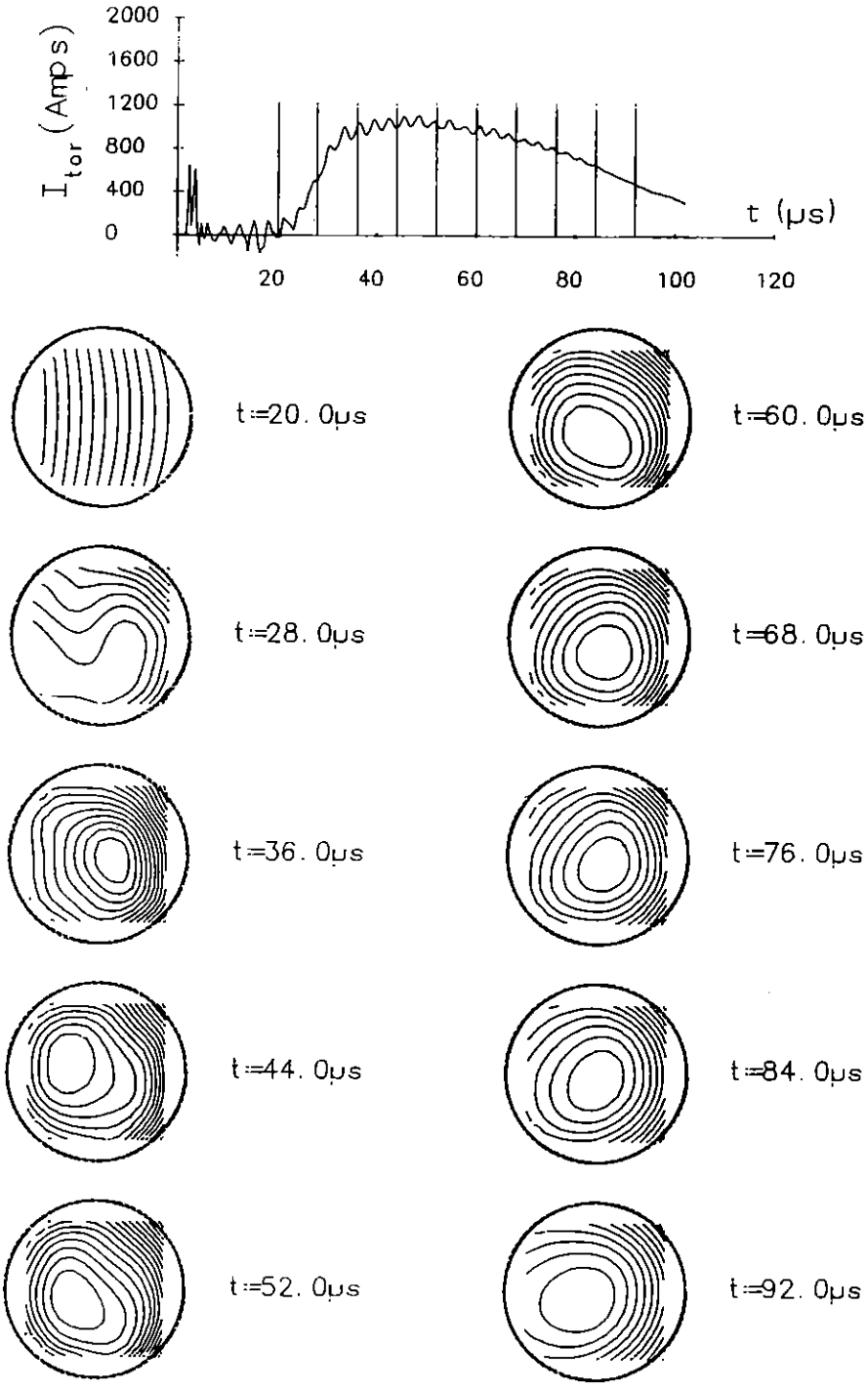

Figure 5.33 Poloidal flux contours for Data Set 13. Vertical field = 10.1G. Contour spacing is $8\pi \times 10^{-6}$ Webers.

of the three experiments. The results of this study (Data Sets 11,12,13) are presented in Figure 5.31, Figure 5.32a and Figure 5.33. Note the dramatic improvement in the number of closed poloidal flux contours under these conditions.

Contour plots of the toroidal current density for Data Set 12 are shown in Figure 5.32b. The toroidal current density is calculated from equation (5.17), using the polynomial coefficients obtained by fitting the raw magnetic probe data. Broken contours are used to indicate regions of negative current density, where the driven current is in the opposite direction to the electromotive force produced by the applied travelling electromagnetic wave.

Three-dimensional plots of the poloidal magnetic flux (Figure 5.32c) and toroidal current density distribution (Figure 5.32d) are provided to assist with interpretation of the two-dimensional contour plots in Figure 5.32a and Figure 5.32b. Interpolation between measurement grid points has been used to improve the presentation of the plots.

Figure 5.32d indicates that a bulk toroidal current is driven during the initial 'start-up' phase of the discharge. At later times during the discharge (e.g. more than 30μs after the start of the RF pulse), the toroidal current density appears to approach a more uniform distribution as predicted by the theory (equation (2.96)). Incomplete penetration of the applied RF magnetic field into the plasma may account for the fact that the toroidal current density retains some hollow character.

5.7.3.7 Current Drive with Partial RF Coil Structures.

In this series of experiments, we examine current drive using a double helix coil structure wound on only one half of the vacuum vessel. The partial toroidal coil structure was observed to drive a substantial amount of toroidal current. The amplitude of the driven toroidal current (with optimum values of the external fields) was approximately

50% of the current measured with the same gas filling pressure when RF current drive was applied over the whole of the discharge vessel (see Data Sets 11–13).

Poloidal flux magnetic probe measurements were performed both underneath (Data Set 14) and well away from the partial antenna (Data Set 15). The poloidal flux contours calculated for each configuration are shown in Figure 5.34a (Data Set 14) and Figure 5.35a (Data Set 15). Toroidal current density contour plots for each experiment are presented in Figure 5.34b and Figure 5.35b respectively.

In Figure 5.36, we present major-radial profiles of the change in the toroidal magnetic field, $\Delta B_{tor}(r, 0)$, associated with the driven poloidal current. As with the poloidal flux contour experiments, measurements were performed both underneath, and well away from, the partial RF coil structure. The profiles were constructed from magnetic probe measurements along the midplane of the device ($z = 0$). The toroidal magnetic field profiles in Figure 5.36 demonstrate that poloidal current is driven strongly underneath the partial antenna, whereas very little poloidal current is driven in the half of the torus which is opposite the RF coil structure.

The magnetic probe measurements for the two experiments were made with the same probe placed at the *same* toroidal location (i.e. using the same array of magnetic probe ports). Rather than physically moving the probe, the experiments were performed by changing the electrical connections in the RF generator loads, so as to feed only one half of the fully toroidal Rythmac-3 $m = 1$ double helix coil structure.

The Rythmac-3 double helix antenna was constructed from four windings whose individual lengths were sufficient to cover half of the torus. The antenna was therefore wound in two halves, each half being connected via a series tuning capacitor as shown in Figure 3.10c. The presence of connections on both halves of the torus made it possible to easily operate each half of the antenna separately. One half of the antenna was wound over both sets of magnetic probe ports and the other half of the antenna was wound on the remaining sections of the vacuum vessel.

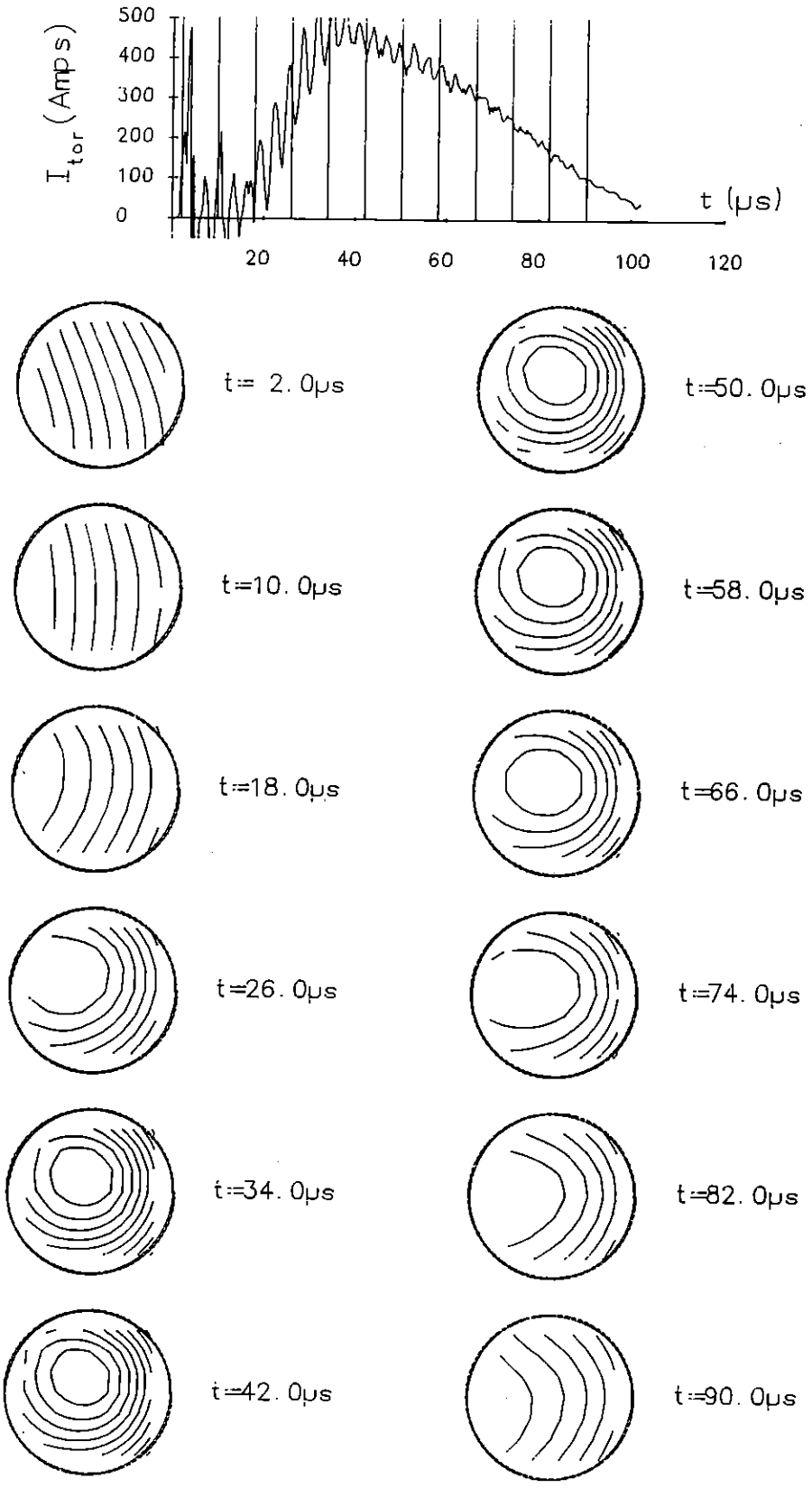

Figure 5.34a Poloidal flux contours for Data Set 14: Underneath partial RF coil structure. Contour spacing is $8\pi \times 10^{-6}$ Webers.

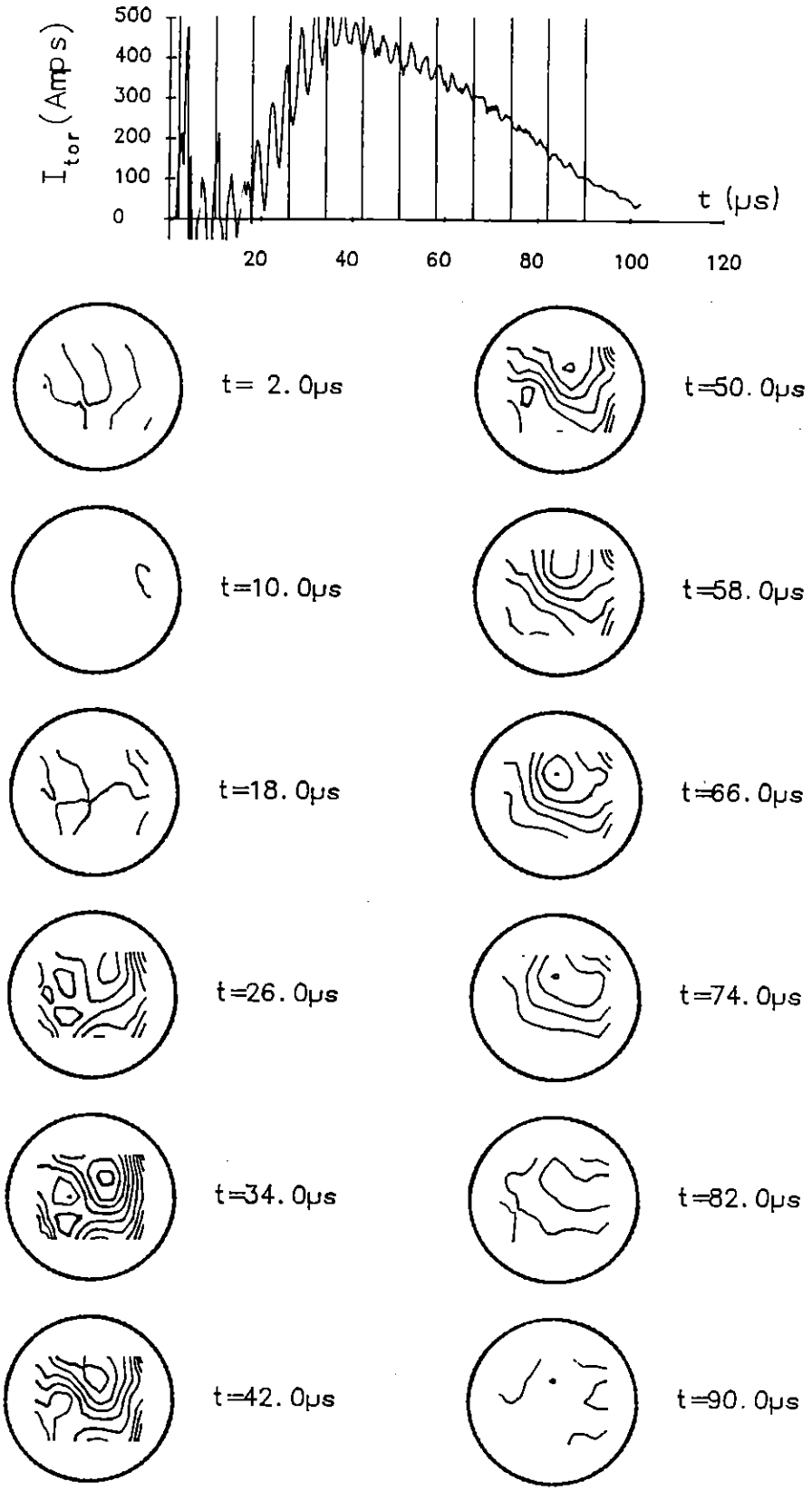

Figure 5.34b Contours of constant toroidal current density for Data Set 14. Broken contours indicate regions of negative current density. The contour spacing is 5000 A/m^2.

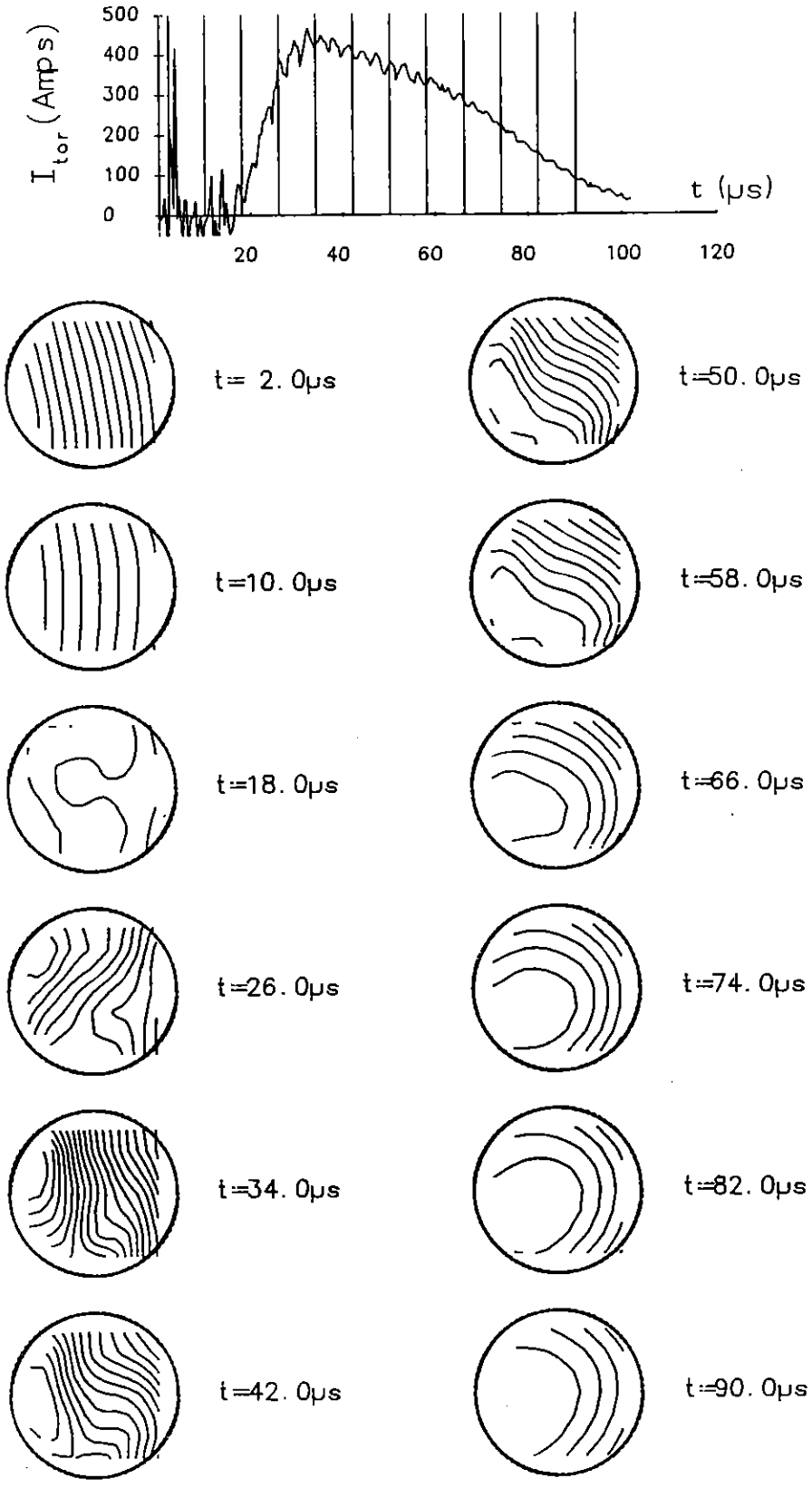

Figure 5.35a Poloidal flux contours for Data Set 15: Opposite partial RF coil structure. Contour spacing is $8\pi \times 10^{-6}$ Webers.

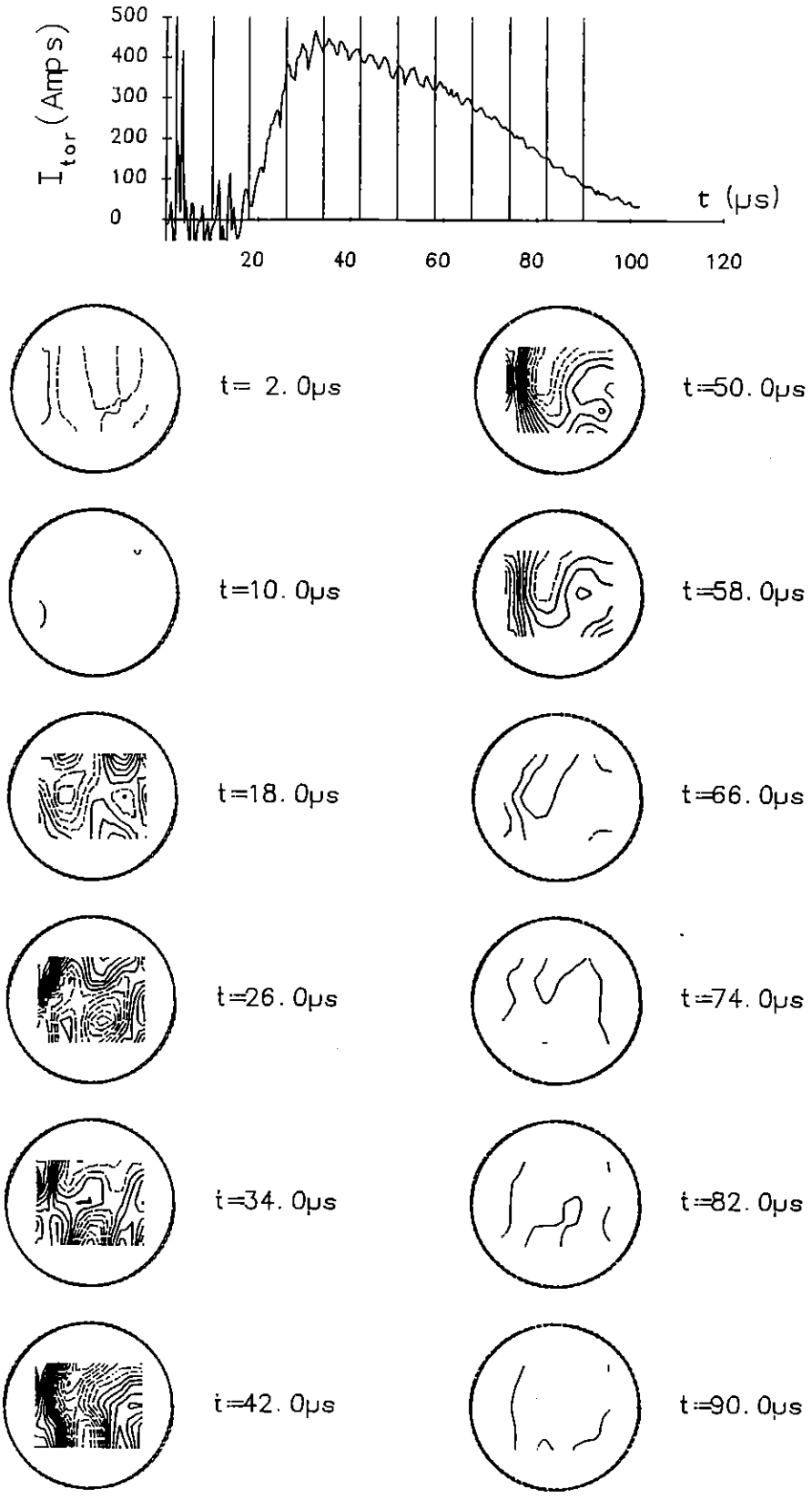

Figure 5.35b Contours of constant toroidal current density for Data Set 15. Broken contours indicate regions of negative current density. The contour spacing is 10000 A/m^2.

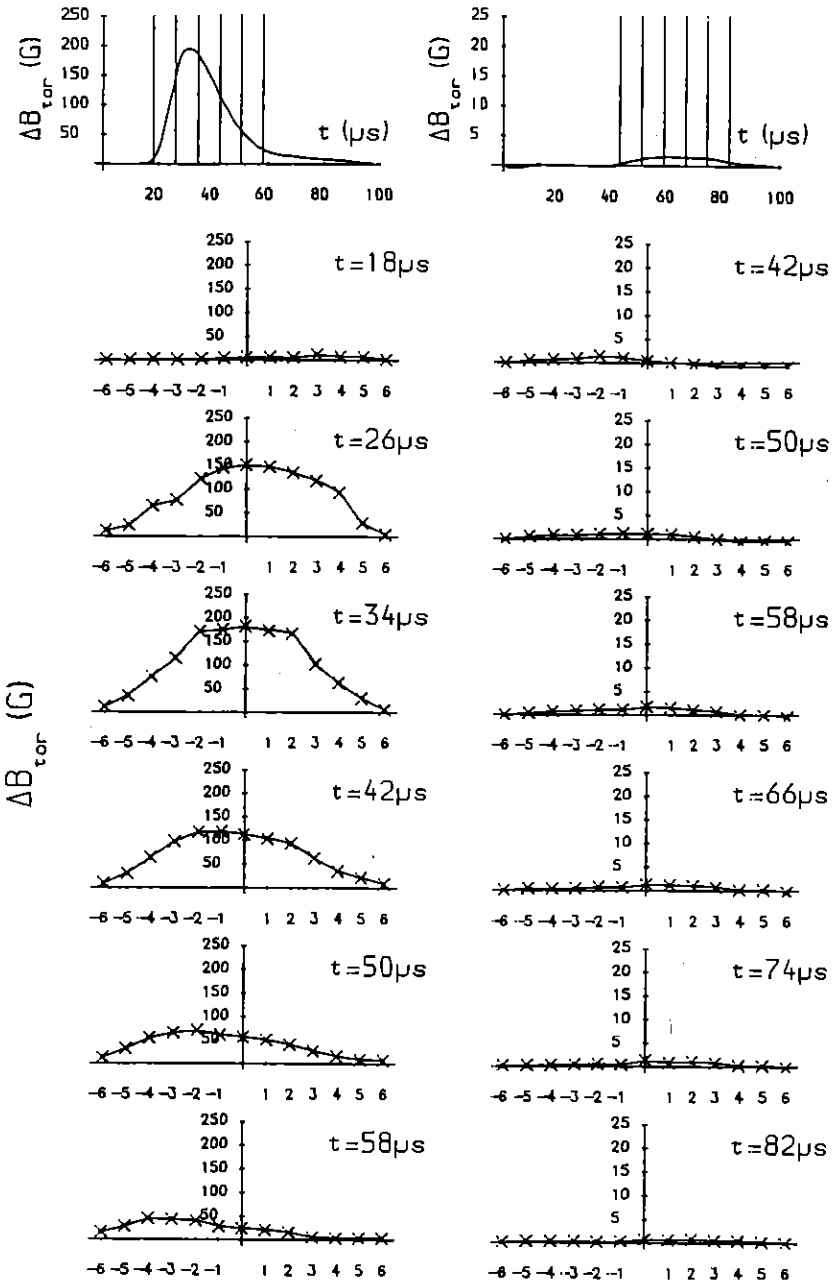

(a) Under RF coils. (b) Opposite RF coils.

Figure 5.36 Radial profiles of the change in toroidal magnetic field associated with the poloidal current driven by the partial RF coil structure, for (a) Data Set 14: probe under RF coil structure and (b) Data Set 15: Opposite half of coil structure fed by RF. The profiles are constructed from raw magnetic probe measurements along the midplane of the device ($z = 0$). In each case, the time dependence of $\Delta B_{tor}(R_0, 0)$, measured with the probe located at the centre of the minor section ($r = R_0, z = 0$) is shown with time markers at the top of the figure. Poloidal current is driven strongly underneath the antenna.